

# Rovibrational energy levels of H<sub>2</sub>O by quantum computing

Erik Lötstedt<sup>1,2,3,\*</sup> and Tamás Szidarovszky<sup>4,†</sup>

<sup>1</sup>*RIKEN Center for Interdisciplinary Theoretical and Mathematical Sciences (iTHEMS), Wako, Saitama 351-0198, Japan*

<sup>2</sup>*Trapped Ion Quantum Computer Team, TRIP Headquarters, RIKEN, Wako, Saitama 351-0198, Japan*

<sup>3</sup>*Computational Condensed Matter Physics Laboratory,*

*RIKEN Pioneering Research Institute (PRI), Wako, Saitama 351-0198, Japan*

<sup>4</sup>*Institute of Chemistry, ELTE Eötvös Loránd University,  
Pázmány Péter Sétány 1/A, H-1117 Budapest, Hungary*

(Dated: March 9, 2026)

We calculate rovibrational energy levels of H<sub>2</sub>O using a trapped-ion quantum computer. We first derive the qubit form of Watson’s Hamiltonian, including the rovibrational coupling terms. In a second step, we employ a variant of the quantum-selected configuration-interaction method to calculate rovibrational energy levels. A truncated form of the qubit Hamiltonian is used to generate correlated rovibrational wave functions on the quantum computer by time evolution, and a basis set is selected by sampling from the measured probability distribution. The rovibrational energy levels are obtained by constructing a Hamiltonian matrix using the selected basis set, and diagonalizing the matrix using a classical computer. We show that an accuracy of a few cm<sup>-1</sup> can be achieved for low-lying rovibrational energy levels.

## I. INTRODUCTION

The electronic structure problem, that is, the calculation of wave functions and energies of the electrons in a molecule, has so far been the main focus of research on quantum computing applied to chemistry [1–12]. Although it is believed that the solution to the electronic structure problem will be one of the main applications for future fault-tolerant quantum computers [13], it is difficult to calculate electronic energies of large molecules using currently available quantum computers due to inherent noise. Thus far, small few-atomic molecules such as Li<sub>2</sub>O [14], F<sub>2</sub> [15], and SrH [16] have been simulated. Recently, larger molecules such as [Fe<sub>4</sub>S<sub>4</sub>(SCH<sub>3</sub>)<sub>4</sub>]<sup>2-</sup> [17, 18] and C<sub>6</sub>H<sub>12</sub> [19] have been treated with hybrid methods where the quantum computer is used to select the active space, and a classical computer is used for the energy evaluation.

On the other hand, to calculate molecular energy levels, we must solve also the Schrödinger equation for the coupled vibrational and rotational motion of the molecule [20]. The solution of the rovibrational Schrödinger equation is a difficult problem: the number of variables  $N_{\text{var}}$  on which the rovibrational wavefunction depends increases linearly with the number of atoms  $N_{\text{a}}$  as  $N_{\text{var}} = 3N_{\text{a}} - 3$ , corresponding to  $3N_{\text{a}} - 6$  vibrational and three rotational coordinates. By using a quantum computer, the hope is that by mapping the rovibrational wave function to qubit form which can be represented on a quantum computer, we can obtain accurate energy levels also for molecules too large to simulate using classical computers. However, compared to the large body of literature on the application of quantum computers to the

electronic structure problem, there are relatively few reports on the application of quantum computers to the rovibrational structure problem. Pioneering studies on the vibrational structure of few-atomic molecules such as O<sub>3</sub> [21, 22] H<sub>2</sub>O [23], CO<sub>2</sub> [24–28], Cr<sub>2</sub> [29] and NH<sub>3</sub> [27, 28] have been carried out. There are also proposals for evaluating the Franck-Condon factors in vibronic transitions [30–34], as well as investigations on the simulation of time-dependent vibrational wave packets [35–37].

In experimental spectroscopy, transitions among rovibrational energy levels of small few-atomic molecules in the gas phase can be measured with very high precision [38–40]. The uncertainty of the wave number of a measured transition is often a fraction of a cm<sup>-1</sup>, and in many cases as small as 10<sup>-6</sup> cm<sup>-1</sup>, where 1 cm<sup>-1</sup> ≈ 0.12 meV ≈ 4.6 × 10<sup>-6</sup> E<sub>h</sub>. “Spectroscopic accuracy” in a theoretical calculation of a rovibrational energy level is commonly referred to as an accuracy of 1 cm<sup>-1</sup> [41, 42]. The experimental transition frequencies are collected in databases such as HITRAN [43, 44], and in the case of well-studied molecules such as H<sub>2</sub>O [45, 46] or NH<sub>3</sub> [47], there are thousands of measured transitions. To interpret the experimental data we must calculate the rovibrational energy levels involved in the transitions, which is a difficult task for a polyatomic molecule. To obtain a good agreement with the experimental data, it is essential to include the coupling between the rotational and vibrational degrees of freedom. However, in previous investigations on vibrational structure evaluation by quantum computing [21–29], the rotational motion of the molecule was not considered. Very recently, Szczepanik and coworkers presented an algorithm for the evaluation of rovibrational wave functions using fault-tolerant quantum computers [48].

In this paper, we aim to calculate rovibrational energy levels using currently available noisy quantum computers, making our investigation complementary to that

\* loetstedte@riken.jp

† tamas.janos.szidarovszky@ttk.elte.hu

for fault-tolerant quantum computers presented in [48]. We derive the qubit form of the rovibrational Hamiltonian and discuss the relative importance of the different terms in the Hamiltonian. Taking the water molecule as an example, we employ the classical-quantum hybrid quantum-selected configuration interaction (QSCI) method [49, 50] and evaluate a number of rovibrational energy levels using the Quantinuum trapped ion quantum computer Reimei [51].

## II. THEORY

### A. Rovibrational Hamiltonian

In this section, we review some parts of rovibrational structure theory. An extensive review can be found in [52].

We consider a nonlinear polyatomic molecule having  $N_{\text{vib}}$  ( $= 3N_a - 6$ ) vibrational normal modes, described by mass-scaled normal-mode coordinates  $Q_1, Q_2, \dots, Q_{N_{\text{vib}}}$  and conjugate momenta  $P_k = -i\hbar\partial/\partial Q_k$ . The rovibrational Hamiltonian, derived by Darling and Dennison [53] and simplified by Watson [54], is defined as

$$H_{\text{W}} = \frac{1}{2}(\mathbf{J} - \boldsymbol{\pi})^T \boldsymbol{\mu} (\mathbf{J} - \boldsymbol{\pi}) + \frac{1}{2} \sum_{k=1}^{N_{\text{vib}}} P_k^2 + V - \frac{\hbar^2}{8} \text{tr}(\boldsymbol{\mu}). \quad (1)$$

In Eq. (1),  $\mathbf{J} = (J_a, J_b, J_c)^T$  is the angular momentum operator in the rotating molecular frame,  $T$  denotes the transpose of a vector,  $\boldsymbol{\pi} = (\pi_a, \pi_b, \pi_c)^T$  is defined in terms of the Coriolis coupling coefficients  $\zeta_{kl}^\alpha$  ( $\alpha = a, b, c$ ) as

$$\pi_\alpha = \sum_{k,l=1}^{N_{\text{vib}}} \zeta_{kl}^\alpha Q_k P_l, \quad (2)$$

$\boldsymbol{\mu}$  is the inverse inertia tensor, and  $V$  is the potential energy surface. We provide detailed definitions and properties of  $\mathbf{J}$ ,  $\zeta_{kl}^\alpha$  and  $\boldsymbol{\mu}$  in Appendix A. The last term proportional to  $\hbar^2$  in the Hamiltonian (1) can be viewed as a quantum correction, because all other terms in (1) appear also in the classical Hamiltonian for a rotating and vibrating molecule [52].

The potential energy surface  $V(Q_1, \dots, Q_{N_{\text{vib}}})$  depends on all the normal mode coordinates in general. In the present investigation, we employ a Taylor expansion up to fourth order in  $Q_k$ ,

$$V(Q_1, \dots, Q_{N_{\text{vib}}}) = V_{\text{harm}} + V_{\text{anharm}}, \quad (3)$$

where

$$V_{\text{harm}} = \frac{1}{2} \sum_{k=1}^{N_{\text{vib}}} \omega_k^2 Q_k^2 \quad (4)$$

is the harmonic part of the potential defined in terms of the mode frequencies  $\omega_k$ , and

$$V_{\text{anharm}} = \frac{1}{6} \sum_{k,l,m=1}^{N_{\text{vib}}} g_{klm} Q_k Q_l Q_m + \frac{1}{24} \sum_{j,k,l,m=1}^{N_{\text{vib}}} f_{jklm} Q_j Q_k Q_l Q_m \quad (5)$$

is the anharmonic part, defined in terms of the anharmonic coupling constants  $g_{klm}$  and  $f_{jklm}$ . We note that in the definition (5), there are many equivalent terms in the sum. For example,  $g_{133} = g_{313} = g_{331}$  and so on.

In order to be consistent with the Taylor expansion of the potential energy, we also expand  $\boldsymbol{\mu}$  up to fourth order in  $Q_k$ ,

$$\boldsymbol{\mu} = \sum_{\ell=0}^4 \boldsymbol{\mu}_\ell, \quad (6)$$

where detailed expressions of the  $\boldsymbol{\mu}_\ell$ 's are given in Eqs. (A8)–(A11) in Appendix A. The actual Hamiltonian used in the simulations,  $H$ , is then defined by collecting all terms in  $H_{\text{W}}$  up to fourth order in  $Q_k$ . To compare the relative importance of the respective terms, we group the terms in  $H$  as follows,

$$H = H_{\text{RR}} + H_{\text{HO}} + V_{\text{anharm}} + H_{\text{vibCor}} + H_{\text{rovib}}, \quad (7)$$

where

$$H_{\text{RR}} = \frac{1}{2} \mathbf{J}^T \boldsymbol{\mu}_0 \mathbf{J} \quad (8)$$

is the rigid-rotor Hamiltonian,

$$H_{\text{HO}} = \frac{1}{2} \sum_{k=1}^{N_{\text{vib}}} P_k^2 + V_{\text{harm}} \quad (9)$$

is the harmonic-oscillator Hamiltonian,  $V_{\text{anharm}}$  is the anharmonic part of the potential energy surface defined in Eq. (5),

$$H_{\text{vibCor}} = \frac{1}{2} \sum_{\ell=0}^2 \boldsymbol{\pi}^T \boldsymbol{\mu}_\ell \boldsymbol{\pi} - \frac{\hbar^2}{8} \sum_{\ell=0}^4 \text{tr} \boldsymbol{\mu}_\ell \quad (10)$$

is the part of the Hamiltonian that describes the vibrational Coriolis coupling (in which we also include the small quantum correction term proportional to  $\hbar^2$ ), and

$$H_{\text{rovib}} = \frac{1}{2} \sum_{\ell=1}^4 \mathbf{J}^T \boldsymbol{\mu}_\ell \mathbf{J} - \sum_{\ell=0}^3 \mathbf{J}^T \boldsymbol{\mu}_\ell \boldsymbol{\pi} \quad (11)$$

is the Hamiltonian describing the coupling of rotation and vibration.

Except for the recent [48], in all previous investigations of quantum computing applied to molecular vibration [21–29], only the  $H_{\text{HO}} + V_{\text{anharm}}$  terms were considered. As we shall see in Sec. III, including also the other terms is essential for obtaining accurate rovibrational energy levels.

## B. Application to H<sub>2</sub>O

The theory reviewed in the previous section II A applies to a general nonlinear polyatomic molecule. In the following, we apply the theory to the triatomic H<sub>2</sub>O molecule as a concrete example. The water molecule has three vibrational modes: symmetric stretch ( $\nu_1$ ), bending ( $\nu_2$ ), and antisymmetric stretch ( $\nu_3$ ). We evaluate the potential energy surface  $V(Q_1, Q_2, Q_3)$  using the CCSD(T) method [55, 56] and the aug-cc-pVQZ basis set [57, 58] implemented in MOLPRO [59–61]. The anharmonic coupling constants  $g_{klm}$  and  $f_{jklm}$  are evaluated using MOLPRO's VPT2 program [62]. We give the numerical values of the relevant parameters in Appendix B.

The rovibrational wave function is expanded as

$$|\Psi\rangle = \sum_{v_1, v_2, v_3=0}^{v_{\max}} \sum_{K=-J}^J c_{v_1 v_2 v_3 K} |v_1 v_2 v_3 K\rangle, \quad (12)$$

where the maximum vibrational quantum number  $v_{\max}$  is assumed to be the same for all three modes,  $c_{v_1 v_2 v_3 K}$  is an expansion coefficient, and the basis state  $|v_1 v_2 v_3 K\rangle$  is defined as a direct product of harmonic oscillator eigenstates  $|v\rangle$  and an angular momentum state  $|J, K\rangle$ ,

$$|v_1 v_2 v_3 K\rangle = |v_1\rangle |v_2\rangle |v_3\rangle |J, K\rangle, \quad (13)$$

where  $K$  measures the projection of the total angular momentum onto the molecular  $c$  axis. The quantum number  $M$  of the projection of the total angular momentum on the lab-frame  $z$  axis is not written out because the Hamiltonian is spherically symmetric and independent of  $M$ . When  $J = 0$ , we omit  $K$  and write  $|v_1 v_2 v_3\rangle \equiv |v_1 v_2 v_3 0\rangle$ . The basis states  $|v_1 v_2 v_3 K\rangle$  are eigenstates of  $H_{\text{HO}}$  but not of the full Hamiltonian  $H$  because of the anharmonic and rovibrational coupling terms. We note that the eigenstates of  $H_{\text{RR}}$ , the asymmetric top rotational wave functions, are superpositions of the rotational basis states  $|J, K\rangle$  [52]. The total angular momentum  $J$  is a constant of motion, so  $J$  is not summed over in Eq. (12). The rovibrational wave functions for different values of  $J$  are calculated independently.

By selecting the  $C_{2v}$  symmetry axis of H<sub>2</sub>O to be the  $c$  axis, the parity under proton exchange is given by

$$P_{\text{ex}} = (-1)^{v_3+K}. \quad (14)$$

This means that states with even  $v_3 + K$  have proton spin  $s = 0$  (para-water), and states with odd  $v_3 + K$  have  $s = 1$  (ortho-water). The Hamiltonian  $H$  does not couple states with different parity  $(-1)^{v_3+K}$ .

We aim to obtain approximate eigenfunctions of  $H$  by solving the eigenvalue problem

$$\mathbf{H}\mathbf{c} = E\mathbf{c}, \quad (15)$$

where  $\mathbf{H}$  is the matrix representation of  $H$  with matrix elements

$$H_{v_1 v_2 v_3 K, v'_1 v'_2 v'_3 K'} = \langle v_1 v_2 v_3 K | H | v'_1 v'_2 v'_3 K' \rangle. \quad (16)$$

For H<sub>2</sub>O, the matrix  $\mathbf{H}$  is of size  $S \times S$ , where  $S = (v_{\max} + 1)^3(2J + 1)$ , and is small enough to diagonalize on a classical computer using standard methods. The motivation to use a quantum computer for the eigenvalue evaluation is that for a molecule having  $N_{\text{vib}}$  vibrational modes,  $S$  scales exponentially with  $N_{\text{vib}}$  as  $S = (v_{\max} + 1)^{N_{\text{vib}}}(2J + 1)$ , which makes it difficult to calculate eigenvalues when  $N_{\text{vib}}$  is large. In the present investigation, H<sub>2</sub>O is selected as a test case where we can obtain the eigenvalues both on classical and quantum computers, so that the accuracy of the quantum algorithm can be assessed in a straightforward way.

The matrix representation  $\mathbf{H}$  of the rovibrational Hamiltonian (16) is a sparse, band-diagonal matrix. The matrix elements  $H_{v_1 v_2 v_3 K, v'_1 v'_2 v'_3 K'}$  are non-zero only when

$$|K - K'| \leq 2 \quad (17)$$

and

$$|v_k - v'_k| \leq 4. \quad (18)$$

The reason for the inequality (17) is that the angular momentum operators  $J_\alpha$  occur at most twice in  $H$ , and (for example)  $\langle J, K | J_a J_b | J, K' \rangle = 0$  when  $|K - K'| > 2$ . The vibrational selection rule (18) derives from the fact that the mode coordinate  $Q_k$  appears at most to fourth order in  $H$ , and  $\langle v | Q^4 | v' \rangle = 0$  for  $|v - v'| > 4$ . The matrix elements of the operator  $\boldsymbol{\pi}^T \boldsymbol{\mu}_\ell \boldsymbol{\pi}$  in Eq. (10) also satisfy  $\langle v | \boldsymbol{\pi}^T \boldsymbol{\mu}_\ell \boldsymbol{\pi} | v' \rangle = 0$  when  $|v - v'| > 4$  because  $\ell \leq 2$  and  $\boldsymbol{\pi}^T \boldsymbol{\mu}_\ell \boldsymbol{\pi}$  therefore contains terms with  $Q_k$  to the power of at most four. We also note that  $\boldsymbol{\pi}$  does not contain terms  $Q_k P_l$  with  $k = l$  [see the definition in Eq. (A3)].

## C. Qubit form of the Hamiltonian

Having established the mathematical form of the Hamiltonian in Eq. (7), we need to derive the qubit form of the Hamiltonian. There are several ways of encoding bosonic degrees of freedom as qubits [63–65]. Here, we use the binary mapping, in which a basis state is mapped to a qubit state according to

$$|v_1 v_2 v_3 K\rangle = |\text{bin}(v_1) \text{bin}(v_2) \text{bin}(v_3) \text{bin}(K)\rangle, \quad (19)$$

where  $\text{bin}(n)$  is the binary representation of the integer  $n$ . This representation requires  $N_q = N_q^{\text{vib}} + N_q^{\text{rot}} = 3[\log_2(v_{\max} + 1)] + \lceil \log_2(2J + 1) \rceil$  qubits, where  $\lceil \cdot \rceil$  denotes the ceiling function. The binary encoding has the advantage of being compact in the sense of requiring a small number of qubits, and can therefore be applied to very large molecules in principle.

The qubit form of the Hamiltonian is given by an expansion

$$H_q = \sum_{\mathbf{k}} h_{\mathbf{k}} P_{\mathbf{k}}, \quad (20)$$

where  $h_{\mathbf{k}}$  is a real-valued coefficient,  $\mathbf{k} = (k_0, k_1, \dots, k_{N_q-1})$  is a composite index ( $k_j \in \{0, 1, 2, 3\}$ ), and  $P_{\mathbf{k}}$  is a direct product of Pauli matrices,

$$P_{\mathbf{k}} = \sigma_{k_{N_q-1}} \otimes \dots \otimes \sigma_{k_1} \otimes \sigma_{k_0}, \quad (21)$$

where  $\sigma_0 = I$ ,  $\sigma_1 = X$ ,  $\sigma_2 = Y$ , and  $\sigma_3 = Z$ . We use  $L_q$  to denote the number of terms having non-zero  $h_{\mathbf{k}}$  in (20).

The numerical values of the  $h_{\mathbf{k}}$  coefficients can be derived by expanding each term in Eq. (7) in terms of  $Q_k$ ,  $P_k$  and  $J_\alpha$ , converting each term to an expression like (20), and combining the expansions. An alternative way, employed in the present investigation, is to evaluate  $h_{\mathbf{k}}$  according to

$$h_{\mathbf{k}} = \frac{1}{2^{N_q}} \text{tr}(P_{\mathbf{k}} \mathbf{H}_q), \quad (22)$$

where the matrix elements of the  $2^{N_q} \times 2^{N_q}$  matrix  $\mathbf{H}_q$  equal those of  $\mathbf{H}$  for all qubit states which represent rovibrational basis states, and equal zero otherwise. The size of  $\mathbf{H}_q$  is larger than that of  $\mathbf{H}$  if  $N_q > 3 \log_2(v_{\max} + 1) + \log_2(2J + 1)$ . Although (22) is easy to use, a naive application requires the evaluation of  $4^{N_q}$  expansion coefficients, which limits the number of qubits to  $N_q < 10$  or so [66].

We have derived the qubit form of the Watson Hamiltonian for  $\text{H}_2\text{O}$  for  $v_{\max} = 1$  and 3, and  $J < 32$ . The number  $L_q$  of terms in the expansion (20) is displayed in Fig. 1(a). We can see that there are many terms in the qubit Hamiltonian. For  $J = 31$  and  $v_{\max} = 3$  ( $N_q = 12$ ), we have  $L_q = 201157$ . Although large,  $L_q$  is still much smaller than the total number of possible 12-qubit Pauli operators,  $4^{12} \approx 1.7 \times 10^7$ . We also see in Fig. 1(a) that  $L_q$  is approximately constant for values of  $J$  resulting in the same number of  $N_q^{\text{rot}}$ . This is a known property of the binary encoding [63, 67]. The variation of  $L_q$  within the range of  $J$  having the same  $N_q^{\text{rot}}$  is too small to be discernible in Fig. 1(a), but is at most a few percent of the average value. For example, for  $v_{\max} = 3$  and  $16 \leq J \leq 31$ , corresponding to  $N_q^{\text{rot}} = 6$ , we have a minimum value of  $L_q^{\text{min}} = 195981$ , a maximum value of  $L_q^{\text{max}} = 208184$ , and an average value of  $\overline{L_q} \approx 204993$ .

In order to get an idea of the scaling of  $L_q$  as a function of  $J$ , we make a least-squares fit of  $L_q$  evaluated at  $J = 2^{N_q^{\text{rot}}-1} - 1$  (that is, the largest  $J$  such that  $2J + 1 < 2^{N_q^{\text{rot}}}$ ) to a power law of the form  $L_q = cJ^\kappa$ . The fits are shown by solid and dotted curves in Fig. 1(a). For both  $v_{\max} = 1$  and  $v_{\max} = 3$ , we find  $\kappa \approx 1$ , showing that  $L_q$  is approximately proportional to  $J$ .

In Fig. 1(b), we show the absolute values  $|h_{\mathbf{k}}|$  of the expansion coefficients for the example of  $J = 1$  for which  $N_q = 8$ . We sort  $|h_{\mathbf{k}}|$  according to size and the number of qubits the corresponding Pauli operator  $P_{\mathbf{k}}$  operates non-trivially on. For example, if  $N_q = 4$ ,  $P = IIXI$  is a one-qubit operator,  $P = IXYZ$  a three-qubit operator, and so on. We can see in Fig. 1(b) that there are many

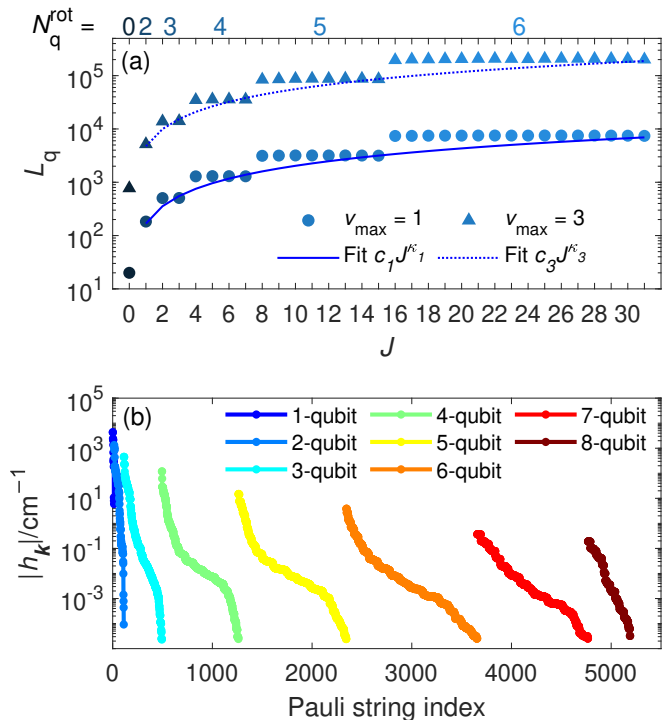


FIG. 1. (a) Number of terms  $L_q$  in the qubit Hamiltonian for  $v_{\max} = 1$  ( $\bullet$ ) and  $v_{\max} = 3$  ( $\blacktriangle$ ). The number of qubits  $N_q^{\text{rot}}$  used to represent the rotational part of the wave function is indicated above the plot. The total number of qubits is  $N_q = N_q^{\text{rot}} + N_q^{\text{vib}} = N_q^{\text{rot}} + 3$  for  $v_{\max} = 1$  and  $N_q = N_q^{\text{rot}} + 6$  for  $v_{\max} = 3$ . The solid and dotted lines represent power-law fits of the form  $L_q = c_{v_{\max}} J^{\kappa_{v_{\max}}}$ , with  $(c_1, \kappa_1) = (167.7, 1.08)$  and  $(c_3, \kappa_3) = (474, 1.07)$ . (b) Absolute values  $|h_{\mathbf{k}}|$  of the expansion coefficients in the qubit Hamiltonian [see Eq. (20)], for  $J = 1$ . The coefficients  $h_{\mathbf{k}}$  are sorted according to size and the number of qubits the Pauli operator  $P_{\mathbf{k}}$  operates on.

terms in  $H_q$  operating on all eight qubits, but that these terms have small absolute values  $|h_{\mathbf{k}}| < 1 \text{ cm}^{-1}$ .

We also comment on the  $v_{\max}$ -dependence of  $L_q$ . For  $J = 0$ , we obtain  $L_q(v_{\max} = 1) = 20$ ,  $L_q(v_{\max} = 3) = 773$  [shown in Fig. 1(a)] and  $L_q(v_{\max} = 7) = 19491$  [not shown in Fig. 1(a)]. As we show in Appendix C, operators of the form  $Q_1^{\ell_1} Q_2^{\ell_2} Q_3^{\ell_3}$  with  $1 \leq \ell_j \leq 4$  have qubit representations where the number of terms scale as  $\mathcal{O}[v_{\max}^3 \log_2^3(v_{\max})]$ . Therefore, we expect the number of terms in  $H_q$  to scale approximately as  $L_q = \mathcal{O}[J v_{\max}^3 \log_2^3(v_{\max})]$  for large  $v_{\max}$ . This scaling holds also for larger molecules with many vibrational modes, assuming that at most three-mode interactions are present in the Hamiltonian.

#### D. Quantum-selected configuration interaction

As can be seen in Fig. 1, the number of terms  $L_q$  in the qubit Hamiltonian is very large. The large value of  $L_q$  means that it is difficult to compute eigenstates

by standard methods like the variation quantum eigensolver (VQE) [68–71]. In the VQE method, we define an ansatz wave function  $|\psi(\boldsymbol{\theta})\rangle$  depending on a number of variational parameters  $\boldsymbol{\theta} = (\theta_1, \theta_2, \dots)$ , and minimize the expectation value of the Hamiltonian  $\langle\psi(\boldsymbol{\theta})|H_q|\psi(\boldsymbol{\theta})\rangle$  with respect to  $\boldsymbol{\theta}$  to find the ground state wave function. However, because one quantum circuit per term in the qubit Hamiltonian has to be executed and measured in order to evaluate the expectation value of the Hamiltonian (the number of circuits can be slightly reduced by grouping the terms into commuting families [72]), and  $\langle\psi(\boldsymbol{\theta})|H_q|\psi(\boldsymbol{\theta})\rangle$  has to be evaluated many times in order to find the optimal value of  $\boldsymbol{\theta}$ , it is not practically feasible to carry out a VQE calculation on current quantum hardware. We comment that the problem of an excessive number of terms in the qubit Hamiltonian is not specific to rovibrational problems. Also electronic structure qubit Hamiltonians have millions of terms in the expansion even for few-atomic molecules (see for example Table II in [73]).

An alternative method for eigenvalue evaluation on quantum computers is the quantum-selected configuration interaction (QSCI) method [49, 50], also referred to as the sample-based quantum diagonalization (SQD) method [17–19]. In the QSCI method, a trial wave function  $|\psi(\boldsymbol{\theta})\rangle$  is prepared using a quantum computer, but unlike the VQE method, the energy is not directly evaluated from  $|\psi(\boldsymbol{\theta})\rangle$ . Instead, we measure  $|\psi(\boldsymbol{\theta})\rangle$  in the computational basis  $|x\rangle$  ( $x = q_{N_q}q_{N_q-1}\dots q_0$  with  $q_j \in \{0, 1\}$ ) to estimate the probability distribution

$$p(x) = |\langle x|\psi(\boldsymbol{\theta})\rangle|^2. \quad (23)$$

Next, we select a subset  $\Omega$  of basis states

$$|x\rangle \in \{|x_1\rangle, |x_2\rangle, \dots\} = \Omega \quad (24)$$

based on the distribution  $p(x)$ . For example, we may select all  $|x\rangle$  such that  $p(x) > \epsilon$  for some threshold value  $\epsilon$ . Approximate eigenstates of  $H_q$  are obtained by diagonalizing the Hamiltonian matrix  $\mathbf{H}_\Omega$  expressed in the  $\Omega$ -basis, having matrix elements

$$H_{\Omega xx'} = \langle x|H_q|x'\rangle, \quad x, x' \in \Omega. \quad (25)$$

The diagonalization is done using a classical computer. The role of the quantum computer is to provide an estimate of the basis functions contributing the most to an eigenstate. The wave function is given in the  $\Omega$ -basis as

$$|\phi\rangle = \sum_{x \in \Omega} c_x |x\rangle, \quad (26)$$

where  $\mathbf{c} = (c_{x_1}, c_{x_2}, \dots)^T$  is an eigenvector of  $\mathbf{H}_\Omega$ . The number of basis states,  $|\Omega|$ , is assumed to be much smaller than the total number  $2^{N_q}$  of qubit states, and to evaluate the eigenvalues, the array of coefficients  $\mathbf{c}$  must fit in the memory of the classical computer. If the basis set is large, complete diagonalization is not carried out;

instead a few low-energy eigenstates are obtained by iterative methods such as the Davidson [74] and Lanczos [75] methods. The QSCI method is expected to work well when an eigenstate of  $H$  is well described using a small subset of states from the entire Hilbert state, as is commonly the case for electronic structure problems [76]. As we shall see in Sec. III C, the QSCI method works rather well also for rovibrational energy levels.

There are various proposals for how to construct the trial wave function  $|\psi(\boldsymbol{\theta})\rangle$ . In [17, 18], a unitary coupled-cluster-type circuit was used. In this paper, we employ a trial wave function constructed by Hamiltonian time evolution [77–80],

$$|\psi(\tau, N_{\text{ST}})\rangle = U^{N_{\text{ST}}}|\psi_0\rangle, \quad (27)$$

where  $N_{\text{ST}}$  is the number of Suzuki-Trotter steps,  $|\psi_0\rangle$  is the initial wave function, and  $U$  is a Suzuki-Trotter approximation [81–83] of the time-evolution operator,

$$U = \prod_{|h_{\mathbf{k}}| > \lambda} e^{-i\tau h_{\mathbf{k}} P_{\mathbf{k}}/\hbar}. \quad (28)$$

In Eq. (28), we have introduced a cutoff parameter  $\lambda$ , meaning that in the time evolution operator  $U$ , we only include terms in the qubit Hamiltonian which have an expansion coefficient  $h_{\mathbf{k}}$  with absolute value larger than  $\lambda$ . In the trial wave function  $|\psi(\tau, N_{\text{ST}})\rangle$  defined in Eqs. (27) and (28), the time step length  $\tau$ , the number of Suzuki-Trotter steps  $N_{\text{ST}}$  and the energy cutoff parameter  $\lambda$  are considered as free (variational) parameters which can be varied to lower the energy. The goal is to prepare a wave function  $|\psi(\tau, N_{\text{ST}})\rangle$  which approximately is composed of the same set of basis functions as the state we are trying to calculate (for example the ground state). The initial state  $|\psi_0\rangle$  in Eq. (27) should be easy to prepare on the quantum computer, and should have a large overlap with the target state.

In the case of the evaluation of rovibrational eigenstates, we are almost always interested in obtaining many eigenstates, not just the ground state. We adopt the approach of selecting a different initial state  $|\psi_0\rangle$  and sampling a different basis set for each excited state. The detailed procedure is given in Sec. III C.

### III. RESULTS

In this section, we present numerical results of the theory described in Sec. II applied to  $\text{H}_2\text{O}$ . The details of our model of  $\text{H}_2\text{O}$  can be found in Appendix B.

#### A. Energy spectrum and the importance of rovibrational coupling

Before the discussion on quantum computing, we start by investigating the spectrum of the rovibrational Hamiltonian. All results in this section III A are obtained using

standard, classical methods. In Table I, we show the energy of the rovibrational ground state  $E_{000}$  ( $J = 0$ ) and the vibrational band origins of the four lowest excited states, that is, the energy difference between the state  $v_1v_2v_3$  and the ground state defined as

$$\Delta E_{v_1v_2v_3} = E_{v_1v_2v_3} - E_{000}. \quad (29)$$

The label  $v_1v_2v_3$  of an eigenstate  $|\phi\rangle$  is decided by the basis state  $|v_1v_2v_3\rangle$  having the largest overlap  $|\langle v_1v_2v_3|\phi\rangle|$  with  $|\phi\rangle$ . This is an unambiguous way of labeling eigenstates for small excitation energies. For large excitation energies above about  $12000 \text{ cm}^{-1}$ , straightforward labeling of the eigenstates becomes difficult because of the pronounced mixing of different basis functions [84].

In Table I, we show the vibrational energies obtained in the harmonic oscillator approximation,

$$E_{v_1v_2v_3}^{\text{HO}} = \sum_{k=1}^3 \left( \frac{1}{2} + v_k \right) \omega_k, \quad (30)$$

by diagonalization of the matrix representation of the full rovibrational Hamiltonian  $H$  using different values of the maximum vibrational quantum number  $v_{\text{max}}$ , and by second-order perturbation theory. In second-order perturbation theory (PT2), we consider the harmonic-oscillator Hamiltonian  $H_{\text{HO}}$  to be the unperturbed Hamiltonian, and the rest of  $H$  to be the perturbation  $H'$ , that is,  $H = H_{\text{HO}} + H'$ . The PT2 vibrational energy is obtained as

$$E_{v_1v_2v_3}^{\text{PT2}} = E_{v_1v_2v_3}^{\text{HO}} + \langle v_1v_2v_3|H'|v_1v_2v_3\rangle + \sum_{\substack{v'_1, v'_2, v'_3=0 \\ v'_1v'_2v'_3 \neq v_1v_2v_3}}^{v_{\text{max}}} \frac{|\langle v_1v_2v_3|H'|v'_1v'_2v'_3\rangle|^2}{E_{v_1v_2v_3}^{\text{HO}} - E_{v'_1v'_2v'_3}^{\text{HO}}}. \quad (31)$$

We mention that in the presence of anharmonic resonances [levels for which the denominator  $E_{v_1v_2v_3}^{\text{HO}} - E_{v'_1v'_2v'_3}^{\text{HO}}$  in (31) is small for some  $v'_1v'_2v'_3$ ], a special treatment is necessary in vibrational perturbation theory [62, 85–87]. The five lowest states shown in Table I are well separated from other states, and Eq. (31) can therefore be used without modification. For reference, we also show the experimentally measured vibrational energies from [45] in Table I.

We make several observations about the data in table I. By comparing the harmonic oscillator energies and the energies obtained using  $H$ , we see that the anharmonic couplings can shift the vibrational energies with more than  $100 \text{ cm}^{-1}$ . Second, the vibrational energies can be considered to be converged at  $v_{\text{max}} = 7$ , although vibrational energies accurate to within about  $30 \text{ cm}^{-1}$  can be obtained already at  $v_{\text{max}} = 3$ . Third, PT2 is not good enough for obtaining accurate eigenenergies. The difference between the  $\Delta E_{v_1v_2v_3}$  obtained using PT2 ( $v_{\text{max}} = 7$ ) and diagonalization of  $\mathbf{H}$  ( $v_{\text{max}} = 7$ ) is larger than  $50 \text{ cm}^{-1}$  for  $\Delta E_{100}$  and  $\Delta E_{001}$ .

TABLE I. Energies in  $\text{cm}^{-1}$  of the vibrational ground state [column labeled by 000], and the vibrational band origins  $\Delta E_{v_1v_2v_3} = E_{v_1v_2v_3} - E_{000}$  [columns with  $v_1v_2v_3 \neq 000$ ] for  $J = 0$ , obtained using the harmonic oscillator approximation, the full rovibrational Hamiltonian  $H$  with different values of  $v_{\text{max}}$ , and second-order perturbation theory [PT2; see the definition in Eq. (31)]. In PT2,  $v_{\text{max}} = 7$  is employed. We also show the experimentally measured energies.

	000	010	020	100	001
HO	4710.5	1649.7	3299.5	3830.9	3940.5
$v_{\text{max}} = 3$	4641.5	1590.2	3162.0	3715.8	3797.0
$v_{\text{max}} = 5$	4640.8	1588.4	3141.6	3688.3	3795.4
$v_{\text{max}} = 7$	4640.8	1588.4	3139.9	3687.8	3795.4
PT2	4628.7	1596.6	3153.4	3630.2	3732.3
Exp. <sup>a</sup>		1594.7	3151.6	3657.1	3755.9

<sup>a</sup> W2020 database [45].

Finally, we note that the difference between the excitation energies obtained in our model of  $\text{H}_2\text{O}$  ( $v_{\text{max}} = 7$ ) and the experimentally measured excitation energies is as large as about  $40 \text{ cm}^{-1}$  for  $\Delta E_{001}$ . In order to reproduce the experimental vibrational energies to within  $1 \text{ cm}^{-1}$ , improved potential energy surfaces combined with more sophisticated basis sets (such as those based on a discrete-variable representation) are required [88, 89]. Curiously, the PT2 energies actually agree better with the experimental values than the energies obtained by diagonalization of  $\mathbf{H}$  [87], even though there is still a discrepancy between PT2 and experiment of more than  $20 \text{ cm}^{-1}$  for  $\Delta E_{100}$  and  $\Delta E_{001}$ .

In Fig. 2(a), we show the rovibrational energy spectrum  $\Delta E$  for  $\Delta E < 6600 \text{ cm}^{-1}$  and  $J$  up to 6, obtained by diagonalization of  $\mathbf{H}$ . The energy  $\Delta E$  is defined as the excitation energy relative to the rovibrational ground state (the lowest energy obtained at  $J = 0$ ). For large values of  $J$ , the density of states becomes large with many close-lying states. For example, for  $J = 6$  and  $\Delta E$  around  $5000 \text{ cm}^{-1}$ , the energy gap between neighboring levels is typically around  $10 \text{ cm}^{-1}$ .

In order to illustrate the importance of the different terms in the Hamiltonian (7), we show in Fig. 2(b) and (c) the energy levels around  $4000 \text{ cm}^{-1}$  for  $J = 0$  and 3 obtained at different levels of approximation. We compare the energy levels obtained using  $H_{\text{RR}} + H_{\text{HO}}$  (harmonic oscillator approximation),  $H_{\text{RR}} + H_{\text{HO}} + V_{\text{anharm}}$  (anharmonic potential energy surface, but no rovibrational coupling),  $H_{\text{RR}} + H_{\text{HO}} + V_{\text{anharm}} + H_{\text{vibCor}}$  (including also vibrational Coriolis coupling), and the full  $H$  (including rovibrational coupling). We can see in Fig. 2(b) and (c) that even if the largest energy change ( $\sim 100 \text{ cm}^{-1}$ ) is due to the inclusion of the anharmonic terms  $V_{\text{anharm}}$  in the Hamiltonian, the vibrational Coriolis coupling  $H_{\text{vibCor}}$  and the rovibrational coupling  $H_{\text{rovib}}$  are crucial for obtaining accurate results. For example, as can be seen in Fig. 2(b) by comparing the “RR + anHO” and “RR + anHO + vibCor” columns, even in the ro-

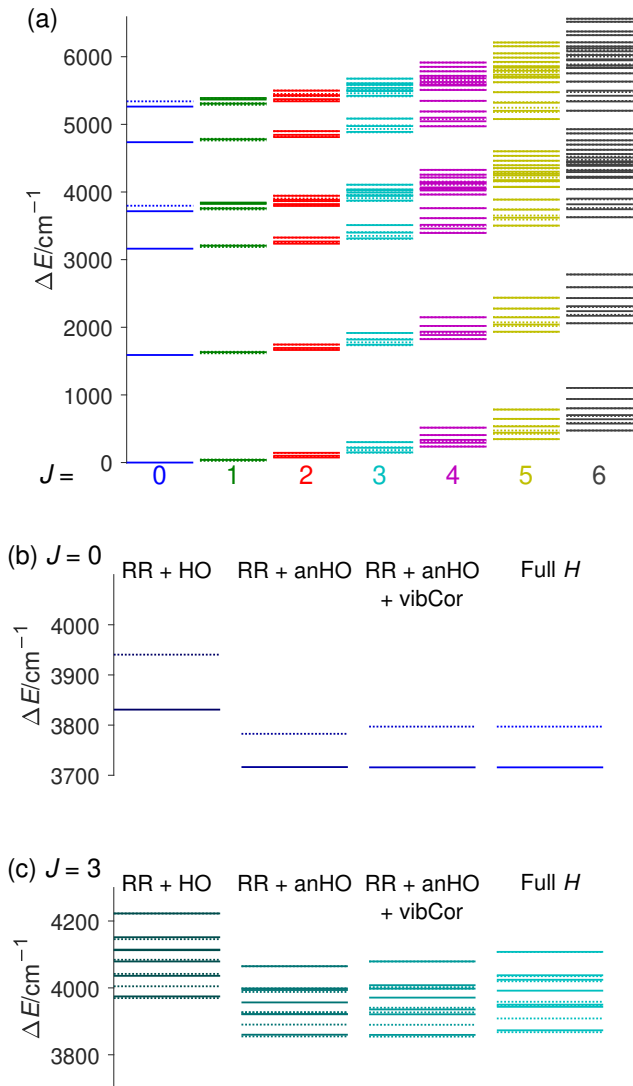


FIG. 2. (a) Rovibrational energy levels  $\Delta E$  relative to the rovibrational ground state for  $0 \leq J \leq 6$  obtained using the full rovibrational Hamiltonian defined in Eq. (7). The maximum vibrational quantum number is  $v_{\max} = 3$ . Energy levels of proton singlet states are drawn by solid lines and triplet states are drawn by dotted lines. (b) Energy spectrum in the range  $3700 \text{ cm}^{-1} \leq \Delta E \leq 4000 \text{ cm}^{-1}$  for  $J = 0$ . We compare the energy levels obtained using the Hamiltonians  $H_{\text{RR}} + H_{\text{HO}}$  (first column),  $H_{\text{RR}} + H_{\text{HO}} + V_{\text{anharm}}$  (second column),  $H_{\text{RR}} + H_{\text{HO}} + V_{\text{anharm}} + H_{\text{vibCor}}$  (third column), and  $H$  (fourth column). See Eqs. (7)–(11) for definitions of the different Hamiltonians. (c) Energy spectrum in the range  $3800 \text{ cm}^{-1} \leq \Delta E \leq 4300 \text{ cm}^{-1}$  for  $J = 3$ .

tational ground state ( $J = 0$ ), the 001 level is shifted from  $\Delta E_{001} = 3782.6 \text{ cm}^{-1}$  by about  $14 \text{ cm}^{-1}$  to  $3797.0 \text{ cm}^{-1}$  by the inclusion of the vibrational Coriolis coupling term. Note that for  $J = 0$ ,  $H_{\text{rovib}} = 0$ , which means that the “Full  $H$ ” energies are the same as the “RR + anHO + vibCor” energies. By comparing the “RR + anHO + vibCor” and the “Full  $H$ ” columns in Fig. 2(c), we can see that for rotating  $\text{H}_2\text{O}$  ( $J = 3$ ), the energy lev-

els around  $4000 \text{ cm}^{-1}$  are shifted by up to  $30 \text{ cm}^{-1}$  by the addition of the rovibrational coupling term  $H_{\text{rovib}}$ . Moreover, the order of the singlet and triplet states are changed for some states.

## B. Distributions by quantum computers

In this section and the next, we describe the results of QSCI calculations. We execute the quantum circuits defined in Eqs. (27) and (28) on Quantinuum’s Reimei quantum computer [51]. Reimei is a 20-qubit trapped-ion quantum computer [90] physically located on the Wako campus of RIKEN, Japan, and features an all-to-all qubit connectivity and a two-qubit gate error of around  $\varepsilon_{2q} = 1 \times 10^{-3}$ . Detailed values of the error rates of Reimei at the time of the simulations are given in Appendix D. The quantum circuits corresponding to  $|\psi(\tau, N_{\text{ST}})\rangle$  are constructed and transpiled using Quantinuum NEXUS [91] and TKET [92].

In Fig. 3, we show two examples of the distribution obtained by measuring the trial wave function  $|\psi(\tau, N_{\text{ST}})\rangle$ . The total angular momentum is  $J = 0$ ,  $v_{\max} = 3$ , and the initial state is  $|\psi_0\rangle = |v_1 = 0, v_2 = 0, v_3 = 0\rangle$  (corresponding to the all-zero qubit state). The total number of qubits employed is  $N_q = 6$ . The cutoff parameter  $\lambda$  in Eq. (28) is taken to be  $\lambda = 110 \text{ cm}^{-1}$ . There are a total of 40 terms (11 single-qubit, 17 two-qubit, 10 three-qubit, and two four-qubit) in the qubit Hamiltonian (20) having  $|h_k| < 110 \text{ cm}^{-1}$ . In Fig. 3(a), we show the result of a simulation run on Reimei on July 18, 2025 employing  $N_{\text{ST}} = 3$  and  $\tau = 0.24 \text{ fs}$  ( $= 10 \text{ a.u.}$ ), and in Fig. 3(b), we show the result of a simulation run on Reimei on November 18, 2025 with  $N_{\text{ST}} = 1$  and  $\tau = 1.5 \text{ fs}$  ( $= 60 \text{ a.u.}$ ). The transpiled circuit for  $|\psi(N_{\text{ST}} = 3, \tau = 0.24 \text{ fs})\rangle$  contains 85  $R_{ZZ}$  two-qubit gates and 134 single-qubit gates. The transpiled circuit for  $|\psi(N_{\text{ST}} = 1, \tau = 1.5 \text{ fs})\rangle$  contains 36  $R_{ZZ}$  gates and 60 single-qubit gates. Three distributions are displayed as a function of the basis function index  $v_1 v_2 v_3$ : (i) the probability distribution of the exact vibrational ground state

$$p_0(v_1 v_2 v_3) = |c_{v_1 v_2 v_3}^0|^2, \quad (32)$$

where  $c^0$  is the lowest-energy eigenvector of  $\mathbf{H}$ , (ii) the exact Suzuki-Trotter distribution

$$p_{\text{ST}}(v_1 v_2 v_3) = |\langle v_1 v_2 v_3 | \psi(\tau, N_{\text{ST}}) \rangle|^2, \quad (33)$$

where  $|\psi(\tau, N_{\text{ST}})\rangle$  is defined in Eqs. (27) and (28), and (iii) the noisy distribution

$$p_{\text{noisy}}(v_1 v_2 v_3) = |\langle v_1 v_2 v_3 | \psi_{\text{noisy}}(\tau, N_{\text{ST}}) \rangle|^2, \quad (34)$$

which is estimated by executing the circuit corresponding to  $|\psi(\tau, N_{\text{ST}})\rangle$  using Reimei. We measure the quantum state  $N_{\text{shot}} = 10^3$  times in order to estimate

$$p_{\text{noisy}}(v_1 v_2 v_3) \approx \frac{N_{v_1 v_2 v_3}}{N_{\text{shot}}}, \quad (35)$$

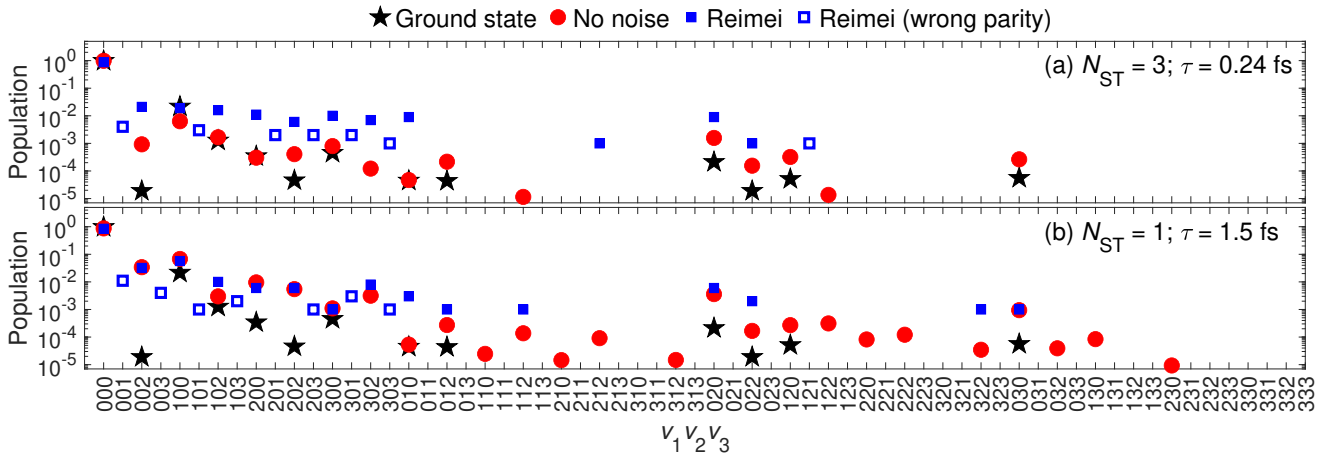


FIG. 3. Distributions of basis states  $|\langle v_1 v_2 v_3 | \psi(\tau, N_{\text{ST}}) \rangle|^2$  for (a)  $N_{\text{ST}} = 3$ ,  $\tau = 0.24$  fs, and (b)  $N_{\text{ST}} = 1$ ,  $\tau = 1.5$  fs. The exact, noise-free distribution is shown with red, filled circles, and the distribution estimated using Reimei ( $N_{\text{shot}} = 10^3$ ) is shown with blue squares. The states having an incorrect value of the parity  $(-1)^{v_3}$  are displayed by open squares. The populations  $|c_{v_1 v_2 v_3}^0|^2$  in the vibrational ground state are shown by black stars as a reference.

where  $N_{v_1 v_2 v_3}$  is the number of measurements of  $|v_1 v_2 v_3\rangle$ . Error mitigation is not applied.

We can see in Figs. 3(a) and (b) that both the exact distribution  $p_{\text{ST}}$  and the noisy distribution  $p_{\text{noisy}}$  are non-zero for basis states which have a non-zero population in the vibrational ground state, which corroborates the idea that the distributions can be used for generation of compact basis sets. The noisy distribution  $p_{\text{noisy}}$  agrees better with  $p_{\text{ST}}$  in Fig. 3(b) than in Fig. 3(a) because of the shorter circuit and the smaller number of noisy two-qubit gates. Because of the finite number of shots ( $N_{\text{shot}} = 10^3$ ) employed in the simulations run on Reimei, some states having small populations in the exact Suzuki-Trotter distribution  $p_{\text{ST}}$  are not present in the Reimei distribution  $p_{\text{noisy}}$ . The Suzuki-Trotter operator  $U$  does not couple basis functions having different parity  $(-1)^{v_3}$ , and therefore basis states where  $v_3$  is odd should not appear in the distribution. However, on Reimei, we measure population in states with odd  $v_3$  (shown with open squares in Fig. 3) due to the noise. When we perform the selection of the basis set by sampling the distribution measured on Reimei, a simple error mitigation procedure consists of post-selecting only the basis functions having the correct parity, and renormalizing the distribution [93–95],

$$p_{\text{mit}}(v_1 v_2 v_3) = \frac{p_{\text{noisy}}(v_1 v_2 v_3)}{\tilde{p}}, \quad (36)$$

where the normalization factor

$$\tilde{p} = \sum_{(-1)^{v_3} = (-1)^{v_3^0}} p_{\text{noisy}}(v_1 v_2 v_3), \quad (37)$$

and  $v_3^0$  is the initial-state vibrational quantum number of mode three.

### C. Rovibrational energy levels by QSCI

In order to evaluate the rovibrational energy levels, we sample from the distributions  $p_{\text{ST}}(v_1 v_2 v_3)$  and  $p_{\text{mit}}(v_1 v_2 v_3)$ . We consider two cases: (i) a fixed value of the time step  $\tau = 10$  a.u. and varying number of Suzuki-Trotter steps  $0 \leq N_{\text{ST}} \leq 10$ , and (ii) fixed  $N_{\text{ST}} = 1$  and varying  $\tau/\text{a.u.} = 0, 20, 40, \dots, 180$ . For each value of  $N_{\text{ST}}$  or  $\tau$ , we collect all basis functions having a population  $p_{\text{mit}}(v_1 v_2 v_3)$  or  $p_{\text{ST}}(v_1 v_2 v_3)$  larger than a threshold value  $\epsilon = 10^{-4}$ . We keep basis functions sampled at previous values of  $N_{\text{ST}}$  or  $\tau$ , and add newly sampled basis functions to the basis set  $\Omega$ . The size  $|\Omega|$  of the basis set increases with  $N_{\text{ST}}$  in case (i), and with  $\tau$  in case (ii). For the simulations done using Reimei, we employ  $N_{\text{shot}} = 10^3$ . This means that all basis states  $|v_1 v_2 v_3\rangle$  with non-zero  $p_{\text{mit}}(v_1 v_2 v_3)$  are added to the basis set, because  $\epsilon < 1/N_{\text{shot}}$ .

With the idea of generating a separate, optimal basis set for each excited state, we generate five basis sets by changing the initial state  $|\psi_0\rangle$ ,

$$|\psi_0(v_1 v_2 v_3)\rangle = |v_1 v_2 v_3\rangle \quad (38)$$

for

$$v_1 v_2 v_3 \in \Gamma = \{000, 010, 020, 100, 001\}. \quad (39)$$

The set  $\Gamma$  represents the five lowest vibrational states. We label the basis set obtained (at certain values of  $N_{\text{ST}}$  and  $\tau$ ) using an initial state  $|\psi_0(v_1 v_2 v_3)\rangle$  by  $\Omega_{v_1 v_2 v_3}$ ,

$$\Omega_{v_1 v_2 v_3} = \{|v_1 v_2 v_3\rangle, |v'_1 v'_2 v'_3\rangle, |v''_1 v''_2 v''_3\rangle, \dots\}. \quad (40)$$

Because the initial state for the generation of  $\Omega_{v_1 v_2 v_3}$  is  $|v_1 v_2 v_3\rangle$ ,  $\Omega_{v_1 v_2 v_3}$  always contains  $|v_1 v_2 v_3\rangle$ , but the other basis functions can be different for each  $\Omega_{v_1 v_2 v_3}$ . For each  $\Omega_{v_1 v_2 v_3}$ , eigenstates  $|\phi_1\rangle, \dots, |\phi_{|\Omega_{v_1 v_2 v_3}|}\rangle$  are obtained by diagonalization of the Hamiltonian matrix  $\mathbf{H}_{\Omega_{v_1 v_2 v_3}}$ .

The estimates of the energy levels is obtained by combining the five basis sets according to the following procedure. From the set of eigenstates generated from the basis set  $\Omega_{v_1 v_2 v_3}$ , we select the eigenstate  $|\phi_{v_1 v_2 v_3}\rangle$  having the largest overlap with the initial state  $|v_1 v_2 v_3\rangle$ . This results in a set of five states  $\{|\phi_{v_1 v_2 v_3}\rangle\}$  with  $v_1 v_2 v_3$  in the range defined in Eq. (39). An orthonormal basis set  $\{|\tilde{\phi}_{v_1 v_2 v_3}\rangle\}$  is produced from  $\{|\phi_{v_1 v_2 v_3}\rangle\}$  by canonical orthogonalization [96], and the final estimates of the energy levels are obtained by diagonalization of the  $5 \times 5$  Hamiltonian matrix with matrix elements  $\langle \tilde{\phi}_{v_1 v_2 v_3} | H | \tilde{\phi}_{v'_1 v'_2 v'_3} \rangle$ . In practice, we find that the absolute values of the off-diagonal elements of the overlap matrix  $\langle \phi_{v_1 v_2 v_3} | \phi_{v'_1 v'_2 v'_3} \rangle$  are smaller than 0.05 for both the basis sets sampled without noise and the basis sets sampled using Reimei, meaning that the original states  $\{|\phi_{v_1 v_2 v_3}\rangle\}$  are close to orthogonal.

We may also consider simply combining the five basis sets  $\Omega_{v_1 v_2 v_3}$  into one large basis set

$$\Omega_{\text{big}} = \bigcup_{v_1 v_2 v_3 \in \Gamma} \Omega_{v_1 v_2 v_3} \quad (41)$$

and computing the energy levels by diagonalization of the Hamiltonian matrix constructed from the basis functions in  $\Omega_{\text{big}}$ . However, because the basis functions in each  $\Omega_{v_1 v_2 v_3}$  are different, the size of  $\Omega_{\text{big}}$  is typically several times larger than the size of each  $\Omega_{v_1 v_2 v_3}$ . As exemplified in Sec. III C 1, using  $\Omega_{\text{big}}$  therefore results in less accurate energy estimates at the same basis set size  $|\Omega_{\text{big}}| \approx |\Omega_{v_1 v_2 v_3}|$ .

We compare the energy levels obtained using quantum computers with the energy levels obtained using two classical methods. In the first method, we calculate the wave function in first-order perturbation theory,

$$|\psi_{\text{PT}}(v_1 v_2 v_3)\rangle = |v_1 v_2 v_3\rangle + |\delta\psi(v_1 v_2 v_3)\rangle, \quad (42)$$

where

$$|\delta\psi(v_1 v_2 v_3)\rangle = \sum_{\substack{v'_1, v'_2, v'_3=0 \\ v'_1 v'_2 v'_3 \neq v_1 v_2 v_3}}^{v_{\text{max}}} \frac{\langle v'_1 v'_2 v'_3 | H' | v_1 v_2 v_3 \rangle}{E_{v_1 v_2 v_3}^{\text{HO}} - E_{v'_1 v'_2 v'_3}^{\text{HO}}} |v'_1 v'_2 v'_3\rangle \quad (43)$$

and the perturbation Hamiltonian  $H'$  is defined as  $H' = H - H_{\text{HO}}$ . The energy levels are obtained by sampling basis functions from the distribution given by the perturbative wave function (43),

$$p_{\text{PT}}(v_1 v_2 v_3) = |\langle v_1 v_2 v_3 | \psi_{\text{PT}}(v_1 v_2 v_3) \rangle|^2, \quad (44)$$

using the same threshold value  $\epsilon = 10^{-4}$  as for the distributions obtained using quantum computers, and diagonalizing the Hamiltonian matrix. Because of the final diagonalization step, this procedure results in more accurate energy estimates than the second-order perturbation theory (31). Moreover, this method is in principle scalable to large systems with many vibrational modes if the sum in (43) is truncated to include only terms with

large values of  $|\langle v'_1 v'_2 v'_3 | H' | v_1 v_2 v_3 \rangle| / (E_{v_1 v_2 v_3}^{\text{HO}} - E_{v'_1 v'_2 v'_3}^{\text{HO}})$ . We note that similar methods of selecting the dominant set of basis functions have been proposed in electronic structure theory, two representative examples being the configuration interaction by perturbation with multiconfigurational zeroth-order wave function selected by iterative process (CIPSI) method [97] and the heat-bath CI method [98]

In the second method, referred to in the following as the ‘‘optimal’’ method, we aim to select the best possible basis set for each state for a given size  $|\Omega|$  of the basis set. We determine the basis sets by adding basis functions one by one as follows. We first fix  $v_1 v_2 v_3$  to one of the states in (39). For  $|\Omega| = 1$ , the basis set consist of only one basis state,  $\Omega_1 = \{|v_1 v_2 v_3\rangle\}$ . In the next step, we add the basis function  $|v'_1 v'_2 v'_3\rangle$  that minimizes the energy of the state  $|\varphi_{v_1 v_2 v_3}\rangle$ , where  $|\varphi_{v_1 v_2 v_3}\rangle$  is defined as the state having the largest overlap with  $|v_1 v_2 v_3\rangle$ . In practice, this means that we test all basis sets  $\{|v_1 v_2 v_3\rangle, |v'_1 v'_2 v'_3\rangle\}$  with  $v'_1 v'_2 v'_3 \neq v_1 v_2 v_3$ , diagonalize the  $2 \times 2$  Hamiltonian matrix and find the basis set which gives the minimum energy of  $|\varphi_{v_1 v_2 v_3}\rangle$ . Next, a basis set with  $|\Omega| = 3$  is constructed by adding a third basis function that minimizes the energy of  $|\varphi_{v_1 v_2 v_3}\rangle$ , and so on. The procedure is repeated for all  $v_1 v_2 v_3$  in (39). To obtain a final, variational estimate of the energies, the basis set  $\{|\varphi_{v_1 v_2 v_3}\rangle\}$ ,  $v_1 v_2 v_3 \in \Gamma$ , is orthogonalized, and the  $5 \times 5$  Hamiltonian matrix with matrix elements  $\langle \varphi_{v_1 v_2 v_3} | H | \varphi_{v'_1 v'_2 v'_3} \rangle$ ,  $v_1 v_2 v_3, v'_1 v'_2 v'_3 \in \Gamma$ , is diagonalized for each value of  $|\Omega|$ . The energies obtained by the optimal method are ideal in the sense that they are close to the best possible estimates of the energy levels which can be obtained with a given basis set size. The optimal method is not scalable to large molecules, but can only be used as a reference method for relatively small molecules and basis sets such as  $\text{H}_2\text{O}$  considered here.

### 1. Vibrational energy levels for $v_{\text{max}} = 3$ and $J = 0$

In Fig. 4, we show the results of rovibrational QSCI simulations carried out on Reimei during July 18–26, 2025. The model parameters employed are  $J = 0$  and  $v_{\text{max}} = 3$  (implying a total number of qubits  $N_{\text{q}} = 6$ ),  $\tau = 0.24$  fs ( $= 10$  a.u.), and a varying number of Suzuki-Trotter steps  $N_{\text{ST}}$ . We show the energy levels for the eigenstates labeled by  $v_1 v_2 v_3$  in  $\Gamma$  [see Eq. (39)], obtained by sampling the distributions (33) and (36). For comparison, we also show result obtained by sampling the perturbation-theory distribution (44), and the energy levels obtained by the optimal method. The energy  $\delta E$  shown in Fig. 4 is defined relative to the exact ground state energy,

$$\delta E_{v_1 v_2 v_3} = E_{v_1 v_2 v_3} - E_{000}^{\text{exact}}, \quad (45)$$

where  $E_{000}^{\text{exact}}$  is the lowest eigenvalue of the full matrix  $\mathbf{H}$  including all  $(v_{\text{max}} + 1)^3 = 64$  basis functions. Note that  $\delta E$  defined in (45) is different from  $\Delta E$  defined in

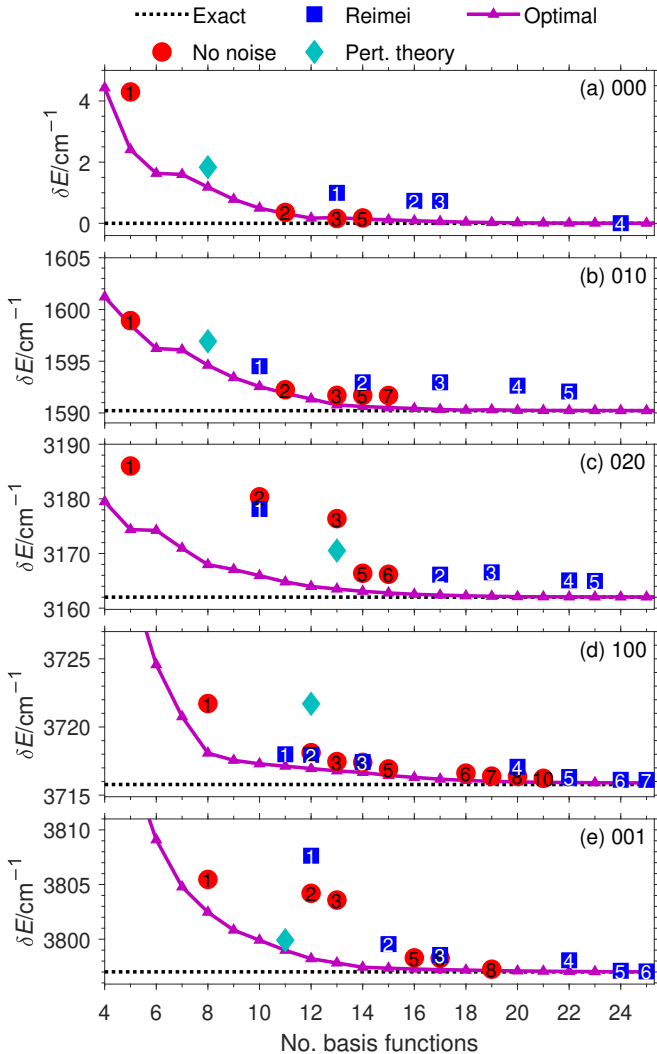


FIG. 4. Energy levels estimates  $\delta E_{v_1 v_2 v_3}$  for  $v_1 v_2 v_3$  equal to (a) 000, (b) 010, (c) 020, (d) 100, and (e) 001, as a function of the number of basis functions in the basis set.  $J = 0$ ,  $v_{\max} = 3$  (corresponding to a number of qubits  $N_q = 6$ ). The values of  $\delta E$  obtained by sampling of the Suzuki-Trotter distribution (36) are shown with filled red circles, those obtained by sampling the mitigated distribution (36) obtained using Reimei are shown with blue, filled squares. The time step size is fixed to  $\tau = 0.24$  fs [same as in Fig. 3(a)], and the number of Suzuki-Trotter steps varies from  $N_{ST} = 0$  to  $N_{ST} = 7$ . The value of  $N_{ST}$  is indicated inside the curve symbols. The energies at  $N_{ST} = 0$  (meaning that the basis set contains only the initial state  $|v_1 v_2 v_3\rangle$ ) are much higher than the largest energies shown in the panels. We have  $\delta E_{000} = 22.5$   $\text{cm}^{-1}$ ,  $\delta E_{010} = 1680.2$   $\text{cm}^{-1}$ ,  $\delta E_{020} = 3241.2$   $\text{cm}^{-1}$ ,  $\delta E_{100} = 4188.6$   $\text{cm}^{-1}$ , and  $\delta E_{001} = 4210.6$   $\text{cm}^{-1}$  for  $N_{ST} = 0$  ( $|\Omega| = 1$ ; same values for the “No noise”, “Reimei” and “Optimal” curves). The exact eigenenergies obtained by diagonalization of  $\mathbf{H}$  are shown with horizontal, dotted lines, the diamond symbol indicates  $\delta E$  obtained by sampling from the perturbation-theory distribution (44), and the  $\delta E$ 's obtained by the optimal method are shown with purple triangles.

(29). Whereas  $\Delta E$  represents an energy difference,  $\delta E$  represents the energy levels directly on a common scale for all methods, which is suitable for a discussion of the convergence with the number of basis functions.

We can see in Fig. 4 that in the noise-free case (filled red circles),  $\delta E$  converges to the exact energy in all cases shown, and becomes close to  $\delta E$  obtained using the optimal method at about  $N_{ST} = 5$  Suzuki-Trotter steps. After one Suzuki-Trotter step ( $N_{ST} = 1$ ), typically five to ten basis functions are sampled. If we consider the largest basis set generated by the sampling (the rightmost red circle in each panel), the difference between the exact energy (horizontal dashed line in Fig. 4) and the energy obtained by noise-free sampling is smaller than  $1$   $\text{cm}^{-1}$  in three cases [(a), (d), and (e)], while we have  $\delta E_{010}^{\text{no noise}}(N_{ST} = 7) - \delta E_{010}^{\text{exact}} \approx 1.5$   $\text{cm}^{-1}$  in Fig. 4(b) and  $\delta E_{020}^{\text{no noise}}(N_{ST} = 6) - \delta E_{020}^{\text{exact}} \approx 4.2$   $\text{cm}^{-1}$  in Fig. 4(c).

Because of the noise, the distribution  $p_{\text{mit}}(v_1 v_2 v_3)$  measured on Reimei is different from the noise-free distribution, as can be seen in Fig. 3. The basis sets sampled on Reimei are larger than in the noise-free case. Typically, 10 to 12 basis functions are sampled after one Suzuki-Trotter step on Reimei. Nevertheless, we can see in Fig. 4 that the Reimei energies converge to energies close to the exact energies. For the rightmost data points shown in Fig. 4, we have  $\delta E_{v_1 v_2 v_3}^{\text{Reimei}} - \delta E_{v_1 v_2 v_3}^{\text{exact}} < 1$   $\text{cm}^{-1}$  in (a), (d), and (e),  $\delta E_{010}^{\text{Reimei}}(N_{ST} = 5) - \delta E_{010}^{\text{exact}} \approx 1.9$   $\text{cm}^{-1}$  in Fig. 4(b), and  $\delta E_{020}^{\text{Reimei}}(N_{ST} = 5) - \delta E_{020}^{\text{exact}} \approx 3.0$   $\text{cm}^{-1}$  in Fig. 4(c).

Due to the finite number of measurements ( $N_{\text{shot}} = 10^3$ ), the basis sets sampled using Reimei have an inherent statistical variation, meaning that if the simulations were repeated at Reimei, basis sets with a slightly different number of basis functions would be generated. In order to assess the variation of the basis sets due to the finite number of measurements, we have repeated the simulations at the same parameters as used in Fig. 4 using Reimei-E, a classical emulator of Reimei [99, 100]. The results, presented in Appendix E, show that while there is a slight variation in the number of basis functions, all simulations using Reimei-E result in data similar to what is shown in Fig. 4.

The energies obtained by sampling the first-order perturbation theory distribution (44), shown by diamonds in Fig. 4, are, at same number of basis functions, sometimes lower than the energies obtained from the Suzuki-Trotter distribution (33) [see Fig. 4(c) and (e)], sometimes comparable [see Fig. 4(a) and (b)], and sometimes higher [see Fig. 4(d)]. This suggests that in many cases, sampling from a distribution determined by perturbation theory is an efficient classical method to generate compact basis sets which may compete with the QSCI method. However, to obtain eigenenergies that differ by less than  $1$   $\text{cm}^{-1}$  from the exact energies, an iterative method (like the electronic structure heat-bath CI method [98]) where the basis set is systematically enlarged would need to be developed.

As a comparison to the results shown in Fig. 4, we have computed the energies using the combined, large basis set as defined in (41). We obtain a basis set size of  $|\Omega_{\text{big}}^{\text{no noise}}| = 24$  and  $|\Omega_{\text{big}}^{\text{Reimei}}| = 37$  at  $N_{\text{ST}} = 1$ . The energies obtained using  $\Omega_{\text{big}}^{\text{no noise}}$  are  $\delta E_{000}^{\text{big; no noise}} = 0.7 \text{ cm}^{-1}$ ,  $\delta E_{010}^{\text{big; no noise}} = 1598.2 \text{ cm}^{-1}$ ,  $\delta E_{020}^{\text{big; no noise}} = 3172.3 \text{ cm}^{-1}$ ,  $\delta E_{100}^{\text{big; no noise}} = 3720.6 \text{ cm}^{-1}$ , and  $\delta E_{001}^{\text{big; no noise}} = 3805.5 \text{ cm}^{-1}$ , which are much larger than the noise-free energies shown in Fig. 4 at  $|\Omega|$  around 15. For Reimei, we obtain  $\delta E_{000}^{\text{big; Reimei}} = 0.0 \text{ cm}^{-1}$ ,  $\delta E_{010}^{\text{big; Reimei}} = 1592.6 \text{ cm}^{-1}$ ,  $\delta E_{020}^{\text{big; Reimei}} = 3163.8 \text{ cm}^{-1}$ ,  $\delta E_{100}^{\text{big; Reimei}} = 3715.9 \text{ cm}^{-1}$ , and  $\delta E_{001}^{\text{big; Reimei}} = 3807.6 \text{ cm}^{-1}$ . In this case, due to the large basis set size, all energies except  $\delta E_{001}$  are of the same accuracy as the Reimei energies in Fig. 4 at  $|\Omega| \approx 20$ .

Some reports [17, 78] compare the energies obtained using QSCI with the energies obtained from a random basis set sampled from a flat distribution. In our case, the basis sets sampled on Reimei are much better than a random basis set. For example, if we define a random basis set of size  $|\Omega_{\text{rand}}|$  as the five basis functions  $|v_1 v_2 v_3\rangle$  with  $v_1 v_2 v_3$  in  $\Gamma$  [see Eq. (39)] combined with  $|\Omega_{\text{rand}}| - 5$  randomly selected basis states, we obtain at  $|\Omega_{\text{rand}}| = 20$  the average energies  $\delta E_{000}^{\text{rand}} = (17 \pm 6) \text{ cm}^{-1}$ ,  $\delta E_{010}^{\text{rand}} = (1658 \pm 6) \text{ cm}^{-1}$ ,  $\delta E_{020}^{\text{rand}} = (3221 \pm 26) \text{ cm}^{-1}$ ,  $\delta E_{100}^{\text{rand}} = (4061 \pm 167) \text{ cm}^{-1}$ , and  $\delta E_{001}^{\text{rand}} = (4098 \pm 150) \text{ cm}^{-1}$ . We have assumed that the same basis set is used for all five states. The statistical uncertainty (the number after the  $\pm$  sign) is estimated as one standard deviation of  $10^3$  randomly sampled basis sets. In all cases, the average energies  $\delta E_{v_1 v_2 v_3}^{\text{rand}}$  are much larger than the energy scale shown in Fig. 4.

## 2. Vibrational energy levels for $v_{\text{max}} = 7$ and $J = 0$

In Fig. 5, we show an example of the vibrational energies at  $J = 0$  obtained with a larger value of the maximum vibrational quantum number  $v_{\text{max}} = 7$ , requiring  $N_{\text{q}}^{\text{vib}} = 3$  qubits per mode and a total of  $N_{\text{q}} = 9$  qubits. The total number of basis states in the full basis set is  $(v_{\text{max}} + 1)^3 = 512$  and the number with correct parity is  $512/2 = 256$ . Differently from the calculation shown in Fig. 4, here we employ a single Suzuki-Trotter step ( $N_{\text{ST}} = 1$ ) and vary the value of the time step  $\tau$ . In order to make the simulation feasible at Reimei, the cutoff parameter in Eq. (28) is set to  $\lambda = 219 \text{ cm}^{-1}$ . There are 146 terms in the qubit Hamiltonian (20) satisfying  $|\hbar_{\mathbf{k}}| < 219 \text{ cm}^{-1}$ : 14 single-qubit, 44 two-qubit, 51 three-qubit, 25 four-qubit, and 12 five-qubit. The simulations using Reimei were carried out during November 21–22 and December 2–3, 2025. The transpiled circuits contain around 280 single-qubit gates and 170 two-qubit  $R_{ZZ}$  gates.

We see in Fig. 5 that the rovibrational QSCI method works rather well also for  $N_{\text{ST}} = 1$  and a larger value of

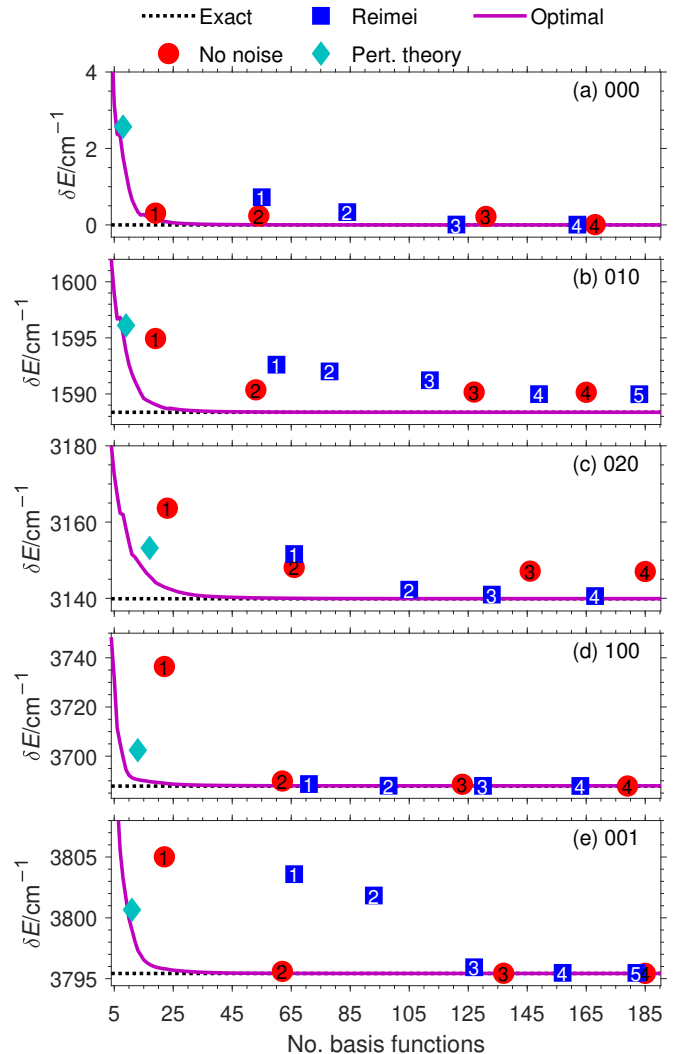


FIG. 5. Energy level estimates  $\delta E_{v_1 v_2 v_3}$  for  $v_1 v_2 v_3$  equal to (a) 000, (b) 010, (c) 020, (d) 100, and (e) 001, as a function of the number of basis functions, for  $J = 0$ ,  $v_{\text{max}} = 7$  ( $N_{\text{q}} = 9$ ). The same curve styles as in Fig. 4 are employed. The number of Suzuki-Trotter steps is fixed to  $N_{\text{ST}} = 1$  and the time step  $\tau = n\tau_0$  with  $\tau_0 = 0.48 \text{ fs}$  and  $n = 0, 1, \dots, 5$  (indicated inside the curve symbols). The energies at  $n = 0$  (only one basis functions) are not shown, and take the values  $\delta E_{000}(n = 0) = 23.3 \text{ cm}^{-1}$ ,  $\delta E_{010}(n = 0) = 1680.0 \text{ cm}^{-1}$ ,  $\delta E_{020}(n = 0) = 3241.9 \text{ cm}^{-1}$ ,  $\delta E_{100}(n = 0) = 4189.4 \text{ cm}^{-1}$ , and  $\delta E_{001}(n = 0) = 4211.4 \text{ cm}^{-1}$  (same values for the “No noise”, “Reimei” and “Optimal” curves).

$v_{\text{max}}$ . The number of sampled basis functions increases with an increasing value of the time step  $\tau$ , with typically around 20 basis functions sampled at the smallest value of  $\tau = 0.48 \text{ fs}$  ( $= 20 \text{ a.u.}$ ) in the noise-free case, and about 65 basis functions for Reimei. At the rightmost data points shown in Fig. 5, we have  $\delta E_{v_1 v_2 v_3}^{\text{no noise}} - \delta E_{v_1 v_2 v_3}^{\text{exact}} < 1 \text{ cm}^{-1}$  in (a), (d), and (e),  $\delta E_{010}^{\text{no noise}}(n = 4) - \delta E_{010}^{\text{exact}} \approx 1.8 \text{ cm}^{-1}$ , and  $\delta E_{020}^{\text{no noise}}(n = 4) - \delta E_{020}^{\text{exact}} \approx 7.1 \text{ cm}^{-1}$ . For the data obtained using Reimei, we have  $\delta E_{v_1 v_2 v_3}^{\text{Reimei}} - \delta E_{v_1 v_2 v_3}^{\text{exact}} < 1 \text{ cm}^{-1}$  in (a), (c), (d), and (e), and

$\delta E_{010}^{\text{Reimei}}(n=5) - \delta E_{010}^{\text{exact}} \approx 1.6 \text{ cm}^{-1}$ . Interestingly, for the  $v_1 v_2 v_3 = 020$  state [see Fig. 5 (c)], the convergence is better for the basis sets sampled using Reimei, indicating that a certain amount of noise can sometimes be helpful for finding suitable basis functions.

### 3. Rovibrational energy levels for $v_{\text{max}} = 3$ and $J = 1$

In this section, we consider the case of a non-zero value of the total angular momentum  $J$ . For the low-energy eigenvalues  $\delta E < 4000 \text{ cm}^{-1}$  we are considering here, the rovibrational eigenstates  $|\phi\rangle$  can be approximated as a product of a vibrational wave function and an asymmetric top rotational wave function  $|\Phi_{J_{K_a K_c}}\rangle$ ,

$$|\phi\rangle \approx |\phi_{\text{vib}}\rangle |\Phi_{J_{K_a K_c}}\rangle. \quad (46)$$

The asymmetric top wave function  $|\Phi_{J_{K_a K_c}}\rangle$  is an eigenfunction of the rigid-rotor Hamiltonian  $H_{\text{RR}}$  [see Eq. (8)], and can be expressed as a superposition of the angular momentum basis functions  $|J, K\rangle$ . For example, for  $J = 1$ , with our definition of the  $c$  axis as the  $C_2$  axis, we have

$$\begin{aligned} |\Phi_{1_{01}}\rangle &= \frac{1}{\sqrt{2}}(|1, 1\rangle + |1, -1\rangle), \\ |\Phi_{1_{11}}\rangle &= |1, 0\rangle, \text{ and} \\ |\Phi_{1_{10}}\rangle &= \frac{1}{\sqrt{2}}(|1, 1\rangle - |1, -1\rangle). \end{aligned} \quad (47)$$

The labels  $J_{K_a K_c}$  on  $|\Phi_{J_{K_a K_c}}\rangle$  are defined by the quantum numbers of the prolate and oblate symmetric top limits (when two rotational constants coincide) [52]. In order of lowest to highest energy, the order of the labels is  $J_{0,J}, J_{1,J}, J_{1,J-1}, J_{2,J-1}, \dots, J_{J-1,1}, J_{J,1}, J_{J,0}$  [52].

Because of Eq. (46), it is reasonable to employ the same basis sets as sampled for  $J = 0$  also for  $J > 0$ . The basis sets for  $J > 0$  are taken to be

$$\Omega_{v_1 v_2 v_3, J} = \{|v'_1 v'_2 v'_3\rangle |K\rangle\}, \quad (48)$$

with

$$|v'_1 v'_2 v'_3\rangle \in \Omega_{v_1 v_2 v_3}, \text{ and } K = -J, \dots, J, \quad (49)$$

where  $\Omega_{v_1 v_2 v_3}$  is a basis set sampled for  $J = 0$  as described in Sec. III C. The size of the basis set is  $|\Omega_{v_1 v_2 v_3, J}| = |\Omega_{v_1 v_2 v_3}|(2J + 1)$ . The eigenenergies are obtained similarly as for  $J = 0$ , that is, we first obtain  $2J + 1$  eigenstates for each basis set  $\Omega_{v_1 v_2 v_3, J}$ , and then combine the eigenstates from all five basis sets into a final basis set which is orthogonalized. The final estimates of the energies are obtained by diagonalizing the  $5(2J+1) \times 5(2J+1)$  Hamiltonian matrix. A rovibrational eigenstate  $|\phi\rangle$  is labeled by  $v_1 v_2 v_3 J_{K_a K_c}$ , determined by the state  $|v_1 v_2 v_3\rangle |\Phi_{J_{K_a K_c}}\rangle$  that has the largest overlap with  $|\phi\rangle$ .

In Fig. 6, we show an example of the above described procedure for  $J = 1$ ,  $v_{\text{max}} = 3$ ,  $\tau = 0.24 \text{ fs}$ , and

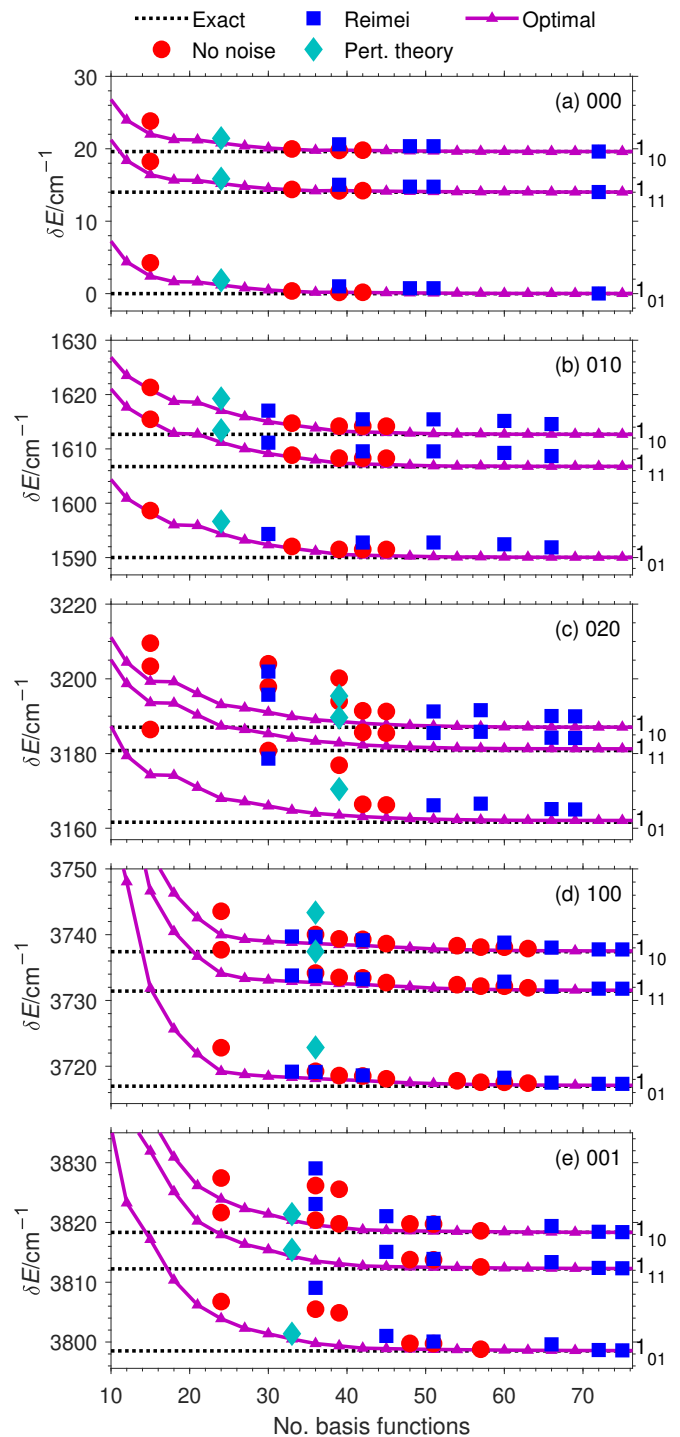


FIG. 6. Rovibrational energy levels for  $J = 1$ , and otherwise the same parameters as in Fig. 4 ( $v_{\text{max}} = 3$ , fixed  $\tau = 0.24 \text{ fs}$ , varying  $N_{\text{ST}}$ ). The value of  $N_{\text{ST}}$  is not shown to avoid cluttering the figure, but is the same as in Fig. 4. For example, in (c), the Reimei data points at  $|\Omega| = 30$  basis functions have  $N_{\text{ST}} = 1$ , the Reimei data points at  $|\Omega| = 69$  have  $N_{\text{ST}} = 5$ . The vibrational state label  $v_1 v_2 v_3$  is indicated in the upper right corner inside each panel, and the rotational state label  $J_{K_a K_c}$  of each level is indicated at the right outside each panel.

$N_{\text{ST}} = 0, 1, \dots, 10$  (the same parameters as in Fig. 4 except for  $J$ ). The total number of basis functions is  $(2J + 1)(v_{\text{max}} + 1)^3 = 192$ . Because  $J = 1$ , there are now  $2J + 1 = 3$  rovibrational states labeled with the same vibrational quantum numbers  $v_1 v_2 v_3$ . The label  $J_{K_a K_c}$  of the corresponding rotational state is indicated at the right of each panel. The proton exchange parity can be expressed in terms of  $v_3$ ,  $K_a$  and  $K_c$  as  $P_{\text{ex}} = (-1)^{v_3 + K_a + K_c}$  [in view of (47), this is consistent with (14)]. Therefore, for  $v_1 v_2 v_3 = 000, 010, 020$ , and  $100$  [Fig. 6(a)–(d)], the  $J_{K_a K_c} = 1_{10}$  and  $1_{01}$  states have proton spin  $s = 1$ , and the  $1_{11}$  has  $s = 0$ , while for  $v_1 v_2 v_3 = 001$  [Fig. 6(e)],  $1_{10}$  and  $1_{01}$  are singlet states and  $1_{11}$  is a triplet state.

Naturally, a similar energy convergence with an increasing number of basis functions as in Fig. 4 is observed in Fig. 6. For the rightmost data points in Fig. 6, we have  $|\delta E_{v_1 v_2 v_3 J_{K_a K_c}}^{\text{exact}} - \delta E_{v_1 v_2 v_3 J_{K_a K_c}}^{\text{no noise}}| < 1 \text{ cm}^{-1}$  in Fig. 6(a), (d), and (e),  $|\delta E_{010 J_{K_a K_c}}^{\text{no noise}} - \delta E_{010 J_{K_a K_c}}^{\text{exact}}| \approx 1.5 \text{ cm}^{-1}$  and  $|\delta E_{010 J_{K_a K_c}}^{\text{Reimei}} - \delta E_{010 J_{K_a K_c}}^{\text{exact}}| \approx 1.9 \text{ cm}^{-1}$  in Fig. 6(b), and  $|\delta E_{020 J_{K_a K_c}}^{\text{no noise}} - \delta E_{020 J_{K_a K_c}}^{\text{exact}}| \approx 4 \text{ cm}^{-1}$  and  $|\delta E_{020 J_{K_a K_c}}^{\text{Reimei}} - \delta E_{020 J_{K_a K_c}}^{\text{exact}}| \approx 3 \text{ cm}^{-1}$  in Fig. 6(c).

The results shown in Fig. 6 demonstrate the Hamiltonian-simulation based rovibrational QSCI method can be used to generate rather compact basis sets for rovibrational states also at non-zero values of the total angular momentum  $J$ .

#### IV. SUMMARY AND OUTLOOK

We have described how to calculate approximate eigenstates of rotating and vibrating molecules using quantum computers. The transformation of the Watson Hamiltonian into qubit form revealed that the qubit Hamiltonian expressed as a linear combination of Pauli strings contains thousands of terms, too many to apply standard quantum computing methods like the VQE. By adopting a variant of the QSCI method, where the basis set is sampled on a quantum computer and the energies are computed classically, we showed that rovibrational energy levels of  $\text{H}_2\text{O}$  can be evaluated to an accuracy of below  $1 \text{ cm}^{-1}$  in many cases.

While our results suggest that current noisy quantum computers may be of use in rovibrational structure calculations, there are many directions left for future investigations. To assess the true strength of the rovibrational QSCI method, we would need to consider large molecules (e.g. benzene [101, 102]) or molecular clusters (such as water clusters [103–105]) requiring large basis sets so that the Hamiltonian matrix becomes too large to be exactly diagonalized. The most efficient qubit mapping and basis set also deserve further attention [65]. We have used a harmonic oscillator basis in this paper, but it is possible that local, grid-type basis sets [48, 64] can be more efficient for current noisy quantum computers.

Rovibrational structure simulations have an advantage

over other types of simulations because we can compare the results of the simulations with high-precision experimental results in a direct way. This suggests that once rovibrational structure calculations can be reliably carried out on quantum computers, they can be suitable for a verifiable quantum advantage in chemistry: A quantum computer is used to calculate rovibrational transitions in a molecule which is too large to treat classically, but for which transition frequencies can be measured by spectroscopic methods to high precision.

#### ACKNOWLEDGMENTS

We thank Xiaoyang Wang and Arata Yamamoto (RIKEN iTHEMS and RIKEN Quantum) for useful comments. We thank Tomoya Okino (RIKEN) and Nathan Lysne (Quantinuum) for providing the data in Appendix D. E. L. is supported by the JSPS (Kakuenhi no. JP24K08336), by NEDO (project JPNP20017), and by the RIKEN TRIP initiative (RIKEN Quantum). T. Sz. is supported by the NKFIH grant NKKP ADVANCED 152731.

#### V. DATA AVAILABILITY

The data supporting the findings of this article are openly available at [106].

#### Appendix A: Definitions of terms in the Watson Hamiltonian

We largely follow [52], although we adopt a slightly different notation for the angular momentum operators. We fix a coordinate system  $\mathbf{r} = (r_a, r_b, r_c)$  in the molecular frame, denote the coordinate of atom  $n$  in the equilibrium geometry of the molecule by  $\mathbf{r}_n^e$ , and an atomic coordinate displaced from the equilibrium by

$$\mathbf{r}_n = \mathbf{r}_n^e + \boldsymbol{\rho}_n, \quad (\text{A1})$$

where  $\mathbf{r}_n^e$  and  $\boldsymbol{\rho}_n$  satisfy the Eckart conditions [107]  $\sum_n m_n \boldsymbol{\rho}_n = \mathbf{0}$  and  $\sum_n m_n \mathbf{r}_n^e \times \boldsymbol{\rho}_n = \mathbf{0}$  ( $m_n$  is the mass of atom  $n$ ). The mass-scaled normal mode coordinates  $Q_k$  are defined as

$$Q_k = \sum_{n=1}^{N_a} \sum_{\alpha=a,b,c} L_{n\alpha,k} \sqrt{m_n} \rho_{n\alpha}, \quad (\text{A2})$$

where  $L_{n\alpha,k}$  is the transformation matrix determined by the condition that the potential energy  $V(Q_1, \dots, Q_{N_{\text{vib}}})$  only contains terms quadratic in  $Q_k$  for small  $Q_k$ .

The Coriolis coupling coefficients are given by

$$\zeta_{kl}^\alpha = \sum_{n=1}^{N_a} \sum_{\beta,\gamma=a,b,c} \varepsilon_{\alpha\beta\gamma} L_{n\beta,k} L_{n\gamma,l}, \quad (\text{A3})$$

where  $\varepsilon_{\alpha\beta\gamma}$  is the Levi-Civita symbol. The  $\zeta_{kl}^\alpha$  matrices are antisymmetric,  $\zeta_{kl}^\alpha = -\zeta_{lk}^\alpha$ .

The inverse inertia tensor  $\boldsymbol{\mu}$  is defined as the inverse of the tensor  $\mathbf{I}'$ ,

$$\boldsymbol{\mu} = \mathbf{I}'^{-1}, \quad (\text{A4})$$

where  $\mathbf{I}'$  has the molecular-frame matrix elements

$$I'_{\alpha\beta} = I_{\alpha\beta} - \sum_{k,l,m=1}^{N_{\text{vib}}} \zeta_{km}^\alpha \zeta_{lm}^\beta Q_k Q_l. \quad (\text{A5})$$

In Eq. A5,  $I_{\alpha\beta}$  is the usual inertia tensor defined using the atomic positions as

$$I_{\alpha\beta} = \sum_{n=1}^{N_a} m_n (\mathbf{r}_n^2 \delta_{\alpha\beta} - r_{n\alpha} r_{n\beta}). \quad (\text{A6})$$

The inertia tensor at the equilibrium geometry is denoted by  $\mathbf{I}^e$  and is defined similarly,

$$I_{\alpha\beta}^e = \sum_{n=1}^{N_a} m_n (\mathbf{r}_n^{e2} \delta_{\alpha\beta} - r_{n\alpha}^e r_{n\beta}^e). \quad (\text{A7})$$

The molecular-frame coordinate system is selected so that  $\mathbf{I}^e$  is diagonal, that is  $I_{\alpha\beta}^e = 0$  for  $\alpha \neq \beta$ . The equilibrium rotational constants for rotation around axis  $\alpha$  is given by  $\hbar^2/(2I_{\alpha\alpha}^e)$ .

The inverse inertia tensor  $\boldsymbol{\mu}$  can be expanded in orders of  $Q_k$  as indicated in Eq. (6). The different orders are given by

$$\boldsymbol{\mu}_\ell = c_\ell \mathbf{I}^{e-\frac{1}{2}} \mathbf{b}^\ell \mathbf{I}^{e-\frac{1}{2}}, \quad (\text{A8})$$

where the coefficients  $c_\ell$  are defined as

$$c_0 = 1, \quad c_1 = -1, \quad c_2 = \frac{3}{4}, \quad c_3 = -\frac{1}{2}, \quad c_4 = \frac{5}{16}, \quad (\text{A9})$$

$$\mathbf{b} = \sum_{k=1}^{N_{\text{vib}}} \mathbf{I}^{e-\frac{1}{2}} \mathbf{a}_k \mathbf{I}^{e-\frac{1}{2}} Q_k, \quad (\text{A10})$$

and the matrix elements of  $\mathbf{a}_k$  are defined as

$$a_{k\alpha\beta} = 2 \sum_{n=1}^{N_a} \sum_{\gamma,\delta=a,b,c} (\delta_{\alpha\beta} \delta_{\gamma\delta} - \delta_{\alpha\delta} \delta_{\beta\gamma}) \sqrt{m_n} r_{n\gamma}^e L_{n\delta,k}. \quad (\text{A11})$$

The angular momentum operators  $J_{a,b,c}$  in the molecular frame satisfy

$$[J_\alpha, J_\beta] = -i\hbar J_\gamma, \quad (\text{A12})$$

where  $(\alpha, \beta, \gamma)$  is a cyclic permutation of  $(a, b, c)$ . The angular momentum states  $|J, K\rangle$  are eigenstates of  $J_c$  and  $\mathbf{J}^2 = J_a^2 + J_b^2 + J_c^2$ ,

$$\begin{aligned} J_c |J, K\rangle &= \hbar K |J, K\rangle, \\ \mathbf{J}^2 |J, K\rangle &= \hbar^2 J(J+1) |J, K\rangle. \end{aligned} \quad (\text{A13})$$

Differently from the lab frame, Eq. (A12) has a minus sign on the right-hand side. This means that for the raising and lowering operators  $J^\pm = J_a \pm iJ_b$ , we have

$$J^\pm |J, K\rangle = \hbar \sqrt{J(J+1) - K(K \mp 1)} |J, K \mp 1\rangle, \quad (\text{A14})$$

that is,  $J^+$  lowers, and  $J^-$  raises the quantum number  $K$ .

## Appendix B: Parameters of H<sub>2</sub>O

We employ the following structural parameters of H<sub>2</sub>O, obtained at the CCSD(T)/aug-cc-pVQZ level using MOLPRO [59–61].

Equilibrium geometry: O–H internuclear distance

$$|\mathbf{r}_\text{O}^e - \mathbf{r}_\text{H}^e| = 1.8121 \text{ a.u.}, \quad (\text{B1})$$

H–O–H bond angle

$$\theta_{\text{OHO}} = 104.368^\circ. \quad (\text{B2})$$

Equilibrium rotational constants:

$$\begin{aligned} A^e &= \frac{\hbar^2}{2I_{aa}^e} = 9.49 \text{ cm}^{-1}, \\ B^e &= \frac{\hbar^2}{2I_{bb}^e} = 27.24 \text{ cm}^{-1}, \text{ and} \\ C^e &= \frac{\hbar^2}{2I_{cc}^e} = 14.57 \text{ cm}^{-1}. \end{aligned} \quad (\text{B3})$$

Note that our definition of the  $a$ ,  $b$  and  $c$  axes is different from the usual convention for asymmetric top molecules, in which the  $a$ ,  $b$  and  $c$  axes are selected so that  $A^e > B^e > C^e$  [52].

Harmonic frequencies (symmetric stretch, bending, antisymmetric stretch):

$$(\omega_1, \omega_2, \omega_3) = (3830.87, 1649.74, 3940.46) \text{ cm}^{-1}. \quad (\text{B4})$$

Anharmonic coupling constants (only non-zero values of terms  $g_{jkl}$  and  $f_{jklm}$  with  $j \leq k \leq l \leq m$  are given):

$$\begin{aligned} g_{133}/(\hbar^{-\frac{3}{2}} \omega_1^{\frac{1}{2}} \omega_3) &= -1822.17 \text{ cm}^{-1}, \\ g_{233}/(\hbar^{-\frac{3}{2}} \omega_2^{\frac{1}{2}} \omega_3) &= -265.63 \text{ cm}^{-1}, \\ g_{111}/(\hbar^{-\frac{3}{2}} \omega_1^{\frac{3}{2}}) &= -1843.08 \text{ cm}^{-1}, \\ g_{112}/(\hbar^{-\frac{3}{2}} \omega_1 \omega_2^{\frac{3}{2}}) &= -73.77 \text{ cm}^{-1}, \\ g_{122}/(\hbar^{-\frac{3}{2}} \omega_1^{\frac{1}{2}} \omega_2) &= 310.01 \text{ cm}^{-1}, \\ g_{222}/(\hbar^{-\frac{3}{2}} \omega_2^{\frac{3}{2}}) &= 264.59 \text{ cm}^{-1}, \end{aligned} \quad (\text{B5})$$

$$\begin{aligned}
f_{3333}/(\hbar^{-2}\omega_3^2) &= 779.10 \text{ cm}^{-1}, \\
f_{1133}/(\hbar^{-2}\omega_1\omega_3) &= 764.90 \text{ cm}^{-1}, \\
f_{1111}/(\hbar^{-2}\omega_1^2) &= 767.10 \text{ cm}^{-1}, \\
f_{1233}/(\hbar^{-2}\omega_1^{\frac{1}{2}}\omega_2^{\frac{1}{2}}\omega_3) &= 118.20 \text{ cm}^{-1}, \\
f_{1112}/(\hbar^{-2}\omega_1^{\frac{3}{2}}\omega_2^{\frac{1}{2}}) &= 62.20 \text{ cm}^{-1}, \\
f_{2233}/(\hbar^{-2}\omega_2\omega_3) &= -368.56 \text{ cm}^{-1}, \\
f_{1122}/(\hbar^{-2}\omega_1\omega_2) &= -305.41 \text{ cm}^{-1}, \\
f_{1222}/(\hbar^{-2}\omega_1^{\frac{1}{2}}\omega_2^{\frac{3}{2}}) &= -154.64 \text{ cm}^{-1}, \\
f_{2222}/(\hbar^{-2}\omega_2^2) &= -52.89 \text{ cm}^{-1}.
\end{aligned} \tag{B6}$$

Note that we have to account for the multiplicity of the equivalent terms when using the above numerical values in Eq. (5). Except for  $f_{2222}$ , the numerical values given in Eqs. (B5) and (B6) agree with the values in table 6 in [87] to within  $20 \text{ cm}^{-1}$ . The value of  $f_{2222}$  is given in [87] as  $\hbar^2 f_{2222}/\omega_2^2 \approx -11 \text{ cm}^{-1}$ . The signs of the coupling constants in Eqs. (B5) and (B6) and table 6 in [87] agree if we redefine the normal mode coordinates as  $Q_1 \rightarrow -Q_1$  and  $Q_2 \rightarrow -Q_2$ .

Normal mode transformation matrix [used in Eqs. (A2), (A3), and (A11)]:

$$\mathbf{L} = \begin{pmatrix} \mathbf{L}_O \\ \mathbf{L}_{H1} \\ \mathbf{L}_{H2} \end{pmatrix}, \tag{B7}$$

where

$$\begin{aligned}
\mathbf{L}_O &= \begin{pmatrix} L_{Oa,1} & L_{Oa,2} & L_{Oa,3} \\ L_{Ob,1} & L_{Ob,2} & L_{Ob,3} \\ L_{Oc,1} & L_{Oc,2} & L_{Oc,3} \end{pmatrix} \\
&= \begin{pmatrix} 0 & 0 & 0 \\ 0 & 0 & -0.2700 \\ 0.1949 & -0.2719 & 0 \end{pmatrix},
\end{aligned} \tag{B8}$$

$$\mathbf{L}_{H1} = \begin{pmatrix} 0 & 0 & 0 \\ 0.5747 & 0.4120 & 0.5379 \\ -0.3883 & 0.5416 & -0.4174 \end{pmatrix}, \tag{B9}$$

and

$$\mathbf{L}_{H2} = \begin{pmatrix} 0 & 0 & 0 \\ -0.5747 & -0.4120 & 0.5379 \\ -0.3883 & 0.5416 & 0.4174 \end{pmatrix}. \tag{B10}$$

$\mathbf{L}$  is dimensionless and satisfies  $\mathbf{L}^T \mathbf{L} = \mathbf{1}$ .

### Appendix C: $v_{\max}$ -dependence of the number of terms in the qubit Hamiltonian

In this section, we investigate the number of terms in the qubit representation of the matrices  $\mathbf{Q}^{(\ell)}$  having matrix elements

$$(\mathbf{Q}^{(\ell)})_{vv'} = \langle v | \mathbf{Q}^{(\ell)} | v' \rangle, \tag{C1}$$

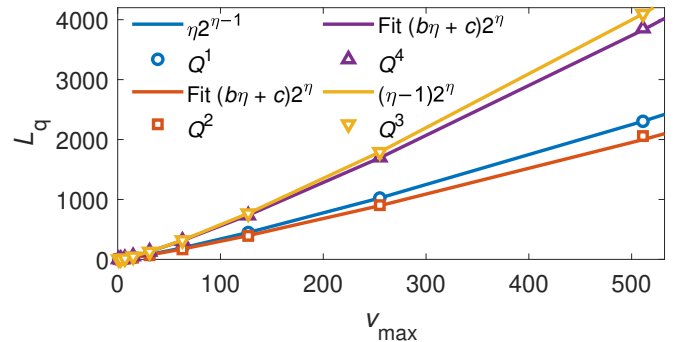


FIG. 7. Open symbols: the number of terms  $L_q$  in the qubit representation of the operator  $Q^\ell$  for  $\ell = 1, 2, 3$ , and  $4$ , as a function of the maximum vibrational quantum number  $v_{\max} = 2^\eta - 1$  ( $\eta = 1, \dots, 9$ ). Solid lines: analytic formulas  $L_q = \eta 2^{\eta-1}$  for  $\ell = 1$ ,  $L_q = (\eta - 1)2^\eta$  for  $\ell = 3$ , and fits to  $L_q = (b\eta + c)2^\eta$  for  $\ell = 2$  and  $4$ . We obtain  $(b, c)_{\ell=2} = (0.402, 0.288)$  and  $(b, c)_{\ell=4} = (0.857, -0.239)$ .

where  $|v\rangle$  is a harmonic-oscillator basis function, and  $Q$  is a normal-mode coordinate. In Fig. 7, we show the number of terms  $L_q$  in the qubit representation of  $\mathbf{Q}^{(\ell)}$ ,

$$\mathbf{Q}^{(\ell)} = \sum_{\mathbf{k}} q_{\mathbf{k}}^{(\ell)} P_{\mathbf{k}}, \tag{C2}$$

where  $q_{\mathbf{k}}^{(\ell)}$  is a numerical coefficient, and  $P_{\mathbf{k}}$  is a direct product of Pauli matrices as defined in Eq. (21). We show  $L_q$  as a function of the maximum value  $v_{\max}$  of the vibrational quantum number, evaluated at values of  $v_{\max}$  such that  $v_{\max} + 1 = 2^\eta$  for  $\eta = 1, 2, \dots, 9$ . In this case, all qubit states represent harmonic oscillator states in the binary mapping.

In [64], it was shown that  $L_q(\mathbf{Q}^{(1)}) = \eta 2^{\eta-1}$ . We find that  $L_q(\mathbf{Q}^{(3)}) = (\eta - 1)2^\eta$  is valid for  $\eta > 1$ . We could not find any analytic formula for  $L_q(\mathbf{Q}^{(2)})$  and  $L_q(\mathbf{Q}^{(4)})$ . As shown in 7,  $L_q(\mathbf{Q}^{(\ell)})$  ( $\ell = 2, 4$ ) can be fitted rather well with the expression  $L_q = (b\eta + c)2^\eta$ . The values of  $b$  and  $c$  are obtained by fitting the numerically evaluated values of  $L_q/2^\eta$  for  $\eta > 1$  to a linear function of  $\eta$ .

Based on the results shown in Fig. 7, we conclude that at least up to  $v_{\max} < 500$ ,  $L_q$  scales with  $v_{\max}$  approximately as  $L_q = \mathcal{O}[v_{\max} \log_2(v_{\max})]$ . For operators involving several modes of the kind  $Q_1^{\ell_1} Q_2^{\ell_2} Q_3^{\ell_3}$ , we have the scaling  $L_q = \mathcal{O}[v_{\max}^3 \log_2^3(v_{\max})]$ .

### Appendix D: Error rates of Reimei

In Table II, we show the error rates of Reimei at the time of the simulations presented in the paper. The dominant error is the two-qubit gate error, which is of the order of  $10^{-3}$  for all simulations. For a more detailed discussion of the error characterization of Quantinuum's quantum computers, see [51] and [108].

TABLE II. Error rates of Reimei at different execution dates: I (July 18–26, 2025), II (November 21–22, 2025), and III (December 2–3, 2025). The value in parentheses indicates the experimental uncertainty.

	I	II	III
1-qubit gate error/ $10^{-5}$	1.8(3)	2.3(3)	2.8(5)
1-qubit leakage error/ $10^{-6}$	2(1)	4(1)	3(1)
2-qubit gate error/ $10^{-3}$	1.35(4)	1.22(5)	1.30(1)
2-qubit leakage error/ $10^{-4}$	1.9(2)	1.6(2)	1.9(1)
Memory error/ $10^{-4}$	2.4(6)	1.3(2)	1.5(2)
Meas. crosstalk error/ $10^{-5}$	1.00(7)	0.5(1)	0.34(4)
SPAM <sup>a</sup> error (av.)/ $10^{-3}$	3.7(2)	4.3(1)	3.7(2)

<sup>a</sup> State preparation and measurement

### Appendix E: Sampling using Reimei-E

In Fig. 8, we show vibrational energy levels at  $J = 0$  and  $v_{\max} = 3$ , obtained by sampling using Reimei-E, a classical emulator of Reimei. In Reimei-E, the simulations are performed on a classical computer using an accurate model of the noise in Reimei [99, 100]. We also show the exact energies obtained by matrix diagonalization and the energies obtained using the optimal method. Each curve symbol in Fig. 8 represents a simulation using Reimei-E and  $N_{\text{shot}} = 10^3$ . We can see that although there are differences in the simulations results due to the statistical nature of the sampling procedure, all simulations eventually converge to the exact energy to within a few  $\text{cm}^{-1}$  at about  $|\Omega| = 20$  basis functions.

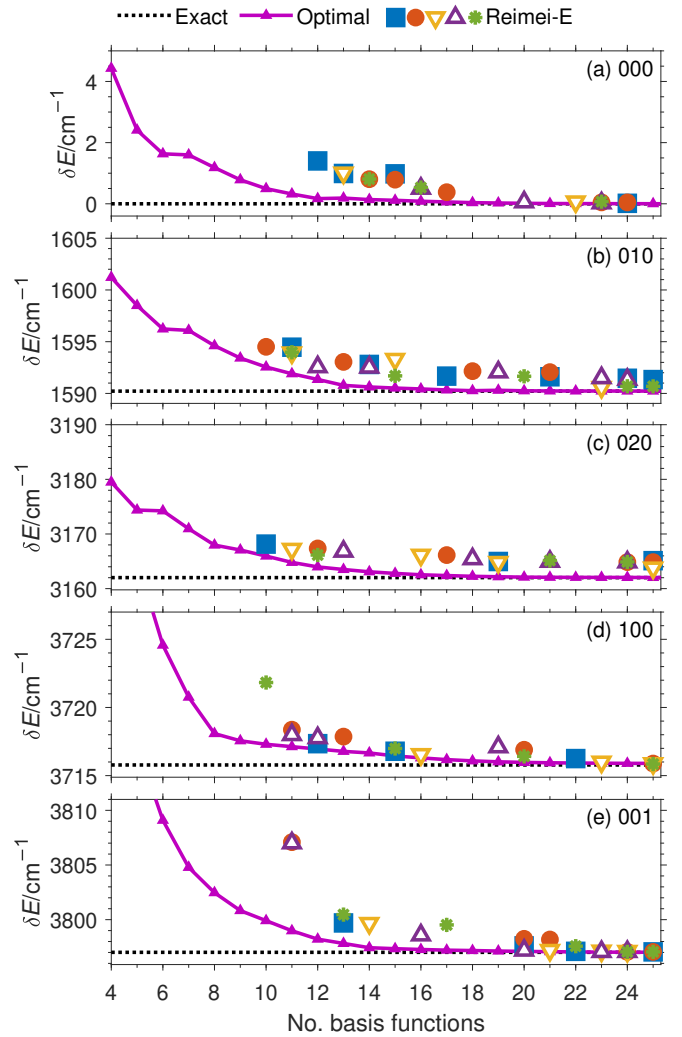


FIG. 8. Vibrational energy levels for  $J = 0$ ,  $v_{\max} = 3$ , fixed  $\tau = 0.24$  fs, and  $1 \leq N_{\text{ST}} \leq 6$ . Each curve symbol ( $\blacksquare$ ,  $\bullet$ ,  $\nabla$ ,  $\triangle$ ,  $*$ ) represents a separate simulation by Reimei-E, with  $N_{\text{shot}} = 10^3$ .

- [1] Y. Cao, J. Romero, J. P. Olson, M. Degroote, P. D. Johnson, M. Kieferová, I. D. Kivlichan, T. Menke, B. Peropadre, N. P. D. Sawaya, S. Sim, L. Veis, and A. Aspuru-Guzik, "Quantum chemistry in the age of quantum computing," *Chem. Rev.* **119**, 10856 (2019).
- [2] B. Bauer, S. Bravyi, M. Motta, and G. K.-L. Chan, "Quantum algorithms for quantum chemistry and quantum materials science," *Chem. Rev.* **120**, 12685 (2020).
- [3] S. McArdle, S. Endo, A. Aspuru-Guzik, S. C. Benjamin, and X. Yuan, "Quantum computational chemistry," *Rev. Mod. Phys.* **92**, 015003 (2020).
- [4] D. Claudino, "The basics of quantum computing for chemists," *Intl. J. Quantum Chem.* **122**, e26990 (2022).
- [5] A. Pyrkov, A. Aliper, D. Bezrukov, Y.-C. Lin, D. Polykovskiy, P. Kamyra, F. Ren, and A. Zhavoronkov, "Quantum computing for near-term applications in generative chemistry and drug discovery," *Drug Discovery Today* **28**, 103675 (2023).
- [6] G. Mazzola, "Quantum computing for chemistry and physics applications from a Monte Carlo perspective," *J. Chem. Phys.* **160**, 010901 (2024).
- [7] J. D. Weidman, M. Sajjan, C. Mikolas, Z. J. Stewart, J. Pollanen, S. Kais, and A. K. Wilson, "Quantum computing and chemistry," *Cell Rep. Phys. Sci.* **5**, 102105 (2024).
- [8] S. Patel, P. Jayakumar, T.-C. Yen, and A. F. Izmaylov, "Quantum measurement for quantum chemistry on a quantum computer," *Chem. Rev.* **125**, 7490 (2025).
- [9] Y. Alexeev, V. S. Batista, N. Bauman, L. Bertels, D. Claudino, R. Dutta, L. Gagliardi, S. Godwin, N. Govind, M. Head-Gordon, M. R. Hermes, K. Kowalski, A. Li, C. Liu, J. Liu, P. Liu, J. M. Garcia-Lastra, D. Mejia-Rodriguez, K. Mueller, M. Otten, B. Peng, M. Raugas, M. Reiher, P. Rigor, W. J. Shaw, M. van Schilfhaarde, T. Vegge, Y. Zhang, M. Zheng, and L. Zhu, "A perspective on quantum computing applications in quantum chemistry using 25–100 logical qubits," *J. Chem. Theory Comput.* **21**, 11335 (2025).
- [10] P. Schleich, L. M. Calderón, C. Sun, M. Bagherimehrab, A. Aldossary, J. S. Kottmann, and A. Aspuru-Guzik, *Quantum Computing for Quantum Chemistry* (American Chemical Society, Washington, D.C., USA, 2025).
- [11] Y. Zhang, X. Zhang, J. Sun, H. Lin, Y. Huang, D. Lv, and X. Yuan, "Quantum algorithms for quantum molecular systems: A survey," *WIREs Comput. Mol. Sci.* **15**, e70020 (2025).
- [12] D. Alfonso, Y.-L. Lee, H. P. Paudel, and Y. Duan, "Chemical applications of variational quantum eigenvalue-based quantum algorithms: Perspective and survey," *Appl. Phys. Rev.* **12**, 031304 (2025).
- [13] A. Katarbarwa, K. Gratsea, A. Caesura, and P. D. Johnson, "Early fault-tolerant quantum computing," *PRX Quantum* **5**, 020101 (2024).
- [14] L. Zhao, J. Goings, K. Shin, W. Kyoung, J. I. Fuks, J.-K. Kevin Rhee, Y. M. Rhee, K. Wright, J. Nguyen, J. Kim, and S. Johri, "Orbital-optimized pair-correlated electron simulations on trapped-ion quantum computers," *npj Quantum Inf.* **9**, 60 (2023).
- [15] S. Guo, J. Sun, H. Qian, M. Gong, Y. Zhang, F. Chen, Y. Ye, Y. Wu, S. Cao, K. Liu, C. Zha, C. Ying, Q. Zhu, H.-L. Huang, Y. Zhao, S. Li, S. Wang, J. Yu, D. Fan, D. Wu, H. Su, H. Deng, H. Rong, Y. Li, K. Zhang, T.-H. Chung, F. Liang, J. Lin, Y. Xu, L. Sun, C. Guo, N. Li, Y.-H. Huo, C.-Z. Peng, C.-Y. Lu, X. Yuan, X. Zhu, and J.-W. Pan, "Experimental quantum computational chemistry with optimized unitary coupled cluster ansatz," *Nat. Phys.* **20**, 1240 (2024).
- [16] P. Chawla, Shweta, K. R. Swain, T. Patel, R. Bala, D. Shetty, K. Sugisaki, S. B. Mandal, J. Riu, J. Nogué, V. S. Prasanna, and B. P. Das, "Relativistic variational-quantum-eigensolver calculations of molecular electric dipole moments on quantum hardware," *Phys. Rev. A* **111**, 022817 (2025).
- [17] J. Robledo-Moreno, M. Motta, H. Haas, A. Javadi-Abhari, P. Jurcevic, W. Kirby, S. Martiel, K. Sharma, S. Sharma, T. Shirakawa, I. Sitdikov, R.-Y. Sun, K. J. Sung, M. Takita, M. C. Tran, S. Yunoki, and A. Mezzacapo, "Chemistry beyond the scale of exact diagonalization on a quantum-centric supercomputer," *Science Advances* **11**, eadu9991 (2025).
- [18] T. Shirakawa, J. Robledo-Moreno, T. Itoko, V. Tripathi, K. Ueda, Y. Kawashima, L. Broers, W. Kirby, H. Pathak, H. Paik, M. Tsuji, Y. Kodama, M. Sato, C. Evangelinos, S. Seelam, R. Walkup, S. Yunoki, M. Motta, P. Jurcevic, H. Horii, and A. Mezzacapo, "Closed-loop calculations of electronic structure on a quantum processor and a classical supercomputer at full scale," (2025), arXiv:2511.00224 [quant-ph].
- [19] A. Shajan, D. Kaliakin, A. Mitra, J. Robledo Moreno, Z. Li, M. Motta, C. Johnson, A. A. Saki, S. Das, I. Sitdikov, A. Mezzacapo, and K. M. Merz, "Toward quantum-centric simulations of extended molecules: Sample-based quantum diagonalization enhanced with density matrix embedding theory," *J. Chem. Theory Comput.* **21**, 6801 (2025).
- [20] A. G. Császár, C. Fábri, T. Szidarovszky, E. Mátyus, T. Furtenbacher, and G. Czako, "The fourth age of quantum chemistry: molecules in motion," *Phys. Chem. Chem. Phys.* **14**, 1085 (2012).
- [21] A. Teplukhin, B. K. Kendrick, and D. Babikov, "Calculation of molecular vibrational spectra on a quantum annealer," *J. Chem. Theory Comput.* **15**, 4555 (2019).
- [22] N. P. D. Sawaya, F. Paesani, and D. P. Tabor, "Near- and long-term quantum algorithmic approaches for vibrational spectroscopy," *Phys. Rev. A* **104**, 062419 (2021).
- [23] S. McArdle, A. Mayorov, X. Shan, S. Benjamin, and X. Yuan, "Digital quantum simulation of molecular vibrations," *Chem. Sci.* **10**, 5725 (2019).
- [24] P. J. Ollitrault, A. Baiardi, M. Reiher, and I. Tavernelli, "Hardware efficient quantum algorithms for vibrational structure calculations," *Chem. Sci.* **11**, 6842 (2020).
- [25] E. Lötstedt, K. Yamanouchi, T. Tsuchiya, and Y. Tachikawa, "Calculation of vibrational eigenenergies on a quantum computer: Application to the Fermi resonance in CO<sub>2</sub>," *Phys. Rev. A* **103**, 062609 (2021).
- [26] E. Lötstedt, K. Yamanouchi, and Y. Tachikawa, "Evaluation of vibrational energies and wave functions of CO<sub>2</sub> on a quantum computer," *AVS Quantum Science* **4**, 036801 (2022).
- [27] M. T. Nguyen, Y.-L. Lee, D. Alfonso, Q. Shao, and Y. Duan, "Description of reaction and vibrational en-

- ergetics of CO<sub>2</sub>-NH<sub>3</sub> interaction using quantum computing algorithms,” *AVS Quantum Science* **5**, 013801 (2023).
- [28] R. Somasundaram, R. Jayaharish, R. Ramanan, and C. Chowdhury, “Quantum computing for molecular vibrational energies: A comprehensive study,” *Mater. Today Quantum* **6**, 100031 (2025).
- [29] K. Asnaashari, D. Bondarenko, and R. V. Krems, “Variational quantum computation with discrete variable representation for ro-vibrational calculations,” (2023), arXiv:2303.09822 [quant-ph].
- [30] J. Huh, G. G. Guerreschi, B. Peropadre, J. R. McClean, and A. Aspuru-Guzik, “Boson sampling for molecular vibronic spectra,” *Nat. Photon.* **9**, 615 (2015).
- [31] Y. Shen, Y. Lu, K. Zhang, J. Zhang, S. Zhang, J. Huh, and K. Kim, “Quantum optical emulation of molecular vibronic spectroscopy using a trapped-ion device,” *Chem. Sci.* **9**, 836 (2018).
- [32] N. P. D. Sawaya and J. Huh, “Quantum algorithm for calculating molecular vibronic spectra,” *J. Phys. Chem. Lett.* **10**, 3586 (2019).
- [33] S. Jahangiri, J. M. Arrazola, N. Quesada, and A. Delgado, “Quantum algorithm for simulating molecular vibrational excitations,” *Phys. Chem. Chem. Phys.* **22**, 25528 (2020).
- [34] C. S. Wang, J. C. Curtis, B. J. Lester, Y. Zhang, Y. Y. Gao, J. Freeze, V. S. Batista, P. H. Vaccaro, I. L. Chuang, L. Frunzio, L. Jiang, S. M. Girvin, and R. J. Schoelkopf, “Efficient multiphoton sampling of molecular vibronic spectra on a superconducting bosonic processor,” *Phys. Rev. X* **10**, 021060 (2020).
- [35] C. Sparrow, E. Martín-López, N. Maraviglia, A. Neville, C. Harrold, J. Carolan, Y. N. Joglekar, T. Hashimoto, N. Matsuda, J. L. O’Brien, D. P. Tew, and A. Laing, “Simulating the vibrational quantum dynamics of molecules using photonics,” *Nature* **557**, 660 (2018).
- [36] C.-K. Lee, C.-Y. Hsieh, S. Zhang, and L. Shi, “Variational quantum simulation of chemical dynamics with quantum computers,” *J. Chem. Theory Comput.* **18**, 2105 (2022).
- [37] S. Malpathak, S. D. Kallullathil, I. Loaiza, S. Fomichev, J. M. Arrazola, and A. F. Izmaylov, “Trotter simulation of vibrational Hamiltonians on a quantum computer,” *J. Chem. Theory Comput.* **22**, 95 (2025).
- [38] M. Quack and F. Merkt, eds., *Handbook of High-resolution Spectroscopy* (Wiley, Hoboken, NJ, USA, 2011).
- [39] V. Shumakova and O. H. Heckl, “A short guide to recent developments in laser-based gas phase spectroscopy, applications, and tools,” *APL Photonics* **9**, 010803 (2024).
- [40] V. Silva de Oliveira, I. Silander, L. Rutkowski, G. Soboń, O. Axner, K. K. Lehmann, and A. Foltynowicz, “Sub-Doppler optical-optical double-resonance spectroscopy using a cavity-enhanced frequency comb probe,” *Nat. Commun.* **15**, 161 (2024).
- [41] K. A. Peterson, D. Feller, and D. A. Dixon, “Chemical accuracy in ab initio thermochemistry and spectroscopy: current strategies and future challenges,” *Theor. Chem. Acc.* **131**, 1079 (2012).
- [42] R. C. Fortenberry, “Quantum astrochemical spectroscopy,” *Int. J. Quantum Chem.* **117**, 81 (2016).
- [43] I. E. Gordon, L. S. Rothman, R. J. Hargreaves, R. Hashemi, E. V. Karlovets, F. M. Skinner, E. K. Conway, C. Hill, R. V. Kochanov, Y. Tan, P. Wcisło, A. A. Finenko, K. Nelson, P. F. Bernath, M. Birk, V. Boudon, A. Campargue, K. V. Chance, A. Coustenis, B. J. Drouin, J.-M. Flaud, R. R. Gamache, J. T. Hodges, D. Jacquemart, E. J. Mlawer, A. V. Nikitin, V. I. Perevalov, M. Rotger, J. Tennyson, G. C. Toon, H. Tran, V. G. Tyuterev, E. M. Adkins, A. Baker, A. Barbe, E. Canè, A. G. Császár, A. Dudaryonok, O. Egorov, A. J. Fleisher, H. Fleurbaey, A. Foltynowicz, T. Furtenbacher, J. J. Harrison, J.-M. Hartmann, V.-M. Horneman, X. Huang, T. Karman, J. Karns, S. Kass, I. Kleiner, V. Kofman, F. Kwabia-Tchana, N. N. Lavrentieva, T. J. Lee, D. A. Long, A. A. Lukashchinskaya, O. M. Lyulin, V. Y. Makhnev, W. Matt, S. T. Massie, M. Melosso, S. N. Mikhailenko, D. Mondelain, H. S. P. Müller, O. V. Naumenko, A. Perrin, O. L. Polyansky, E. Raddaoui, P. L. Raston, Z. D. Reed, M. Rey, C. Richard, R. Tóbiás, I. Sadiq, D. W. Schwenke, E. Starikova, K. Sung, F. Tamassia, S. A. Tashkun, J. Vander Auwera, I. A. Vasilenko, A. A. Viganò, G. L. Villanueva, B. Vispoel, G. Wagner, A. Yachmenev, and S. N. Yurchenko, “The HITRAN2020 molecular spectroscopic database,” *J. Quant. Spectrosc. Radiat. Transfer* **277**, 107949 (2022).
- [44] I. E. Gordon, L. S. Rothman, R. J. Hargreaves, F. M. Gomez, T. Bertin, C. Hill, R. V. Kochanov, Y. Tan, P. Wcisło, V. Y. Makhnev, P. F. Bernath, M. Birk, V. Boudon, A. Campargue, A. Coustenis, B. J. Drouin, R. R. Gamache, J. T. Hodges, D. Jacquemart, E. J. Mlawer, A. V. Nikitin, V. I. Perevalov, M. Rotger, S. Robert, J. Tennyson, G. C. Toon, H. Tran, V. G. Tyuterev, E. M. Adkins, A. Barbe, D. M. Bailey, K. Bielska, L. Bizzocchi, T. A. Blake, C. A. Bowesman, P. Cacciani, P. Čermák, A. G. Császár, L. Denis, S. C. Egbert, O. Egorov, A. Y. Ermilov, A. J. Fleisher, H. Fleurbaey, A. Foltynowicz, T. Furtenbacher, M. Germann, E. R. Guest, J. J. Harrison, J.-M. Hartmann, A. Hjältén, S.-M. Hu, X. Huang, T. J. Johnson, H. Jóźwiak, S. Kass, M. V. Khan, F. Kwabia-Tchana, T. J. Lee, D. Lisak, A.-W. Liu, O. M. Lyulin, N. A. Malarich, L. Manceron, A. A. Marinina, S. T. Massie, J. Mascio, E. S. Medvedev, V. V. Meshkov, G. C. Mellau, M. Melosso, S. N. Mikhailenko, D. Mondelain, H. S. P. Müller, M. O’Donnell, A. Owens, A. Perrin, O. L. Polyansky, P. L. Raston, Z. D. Reed, M. Rey, C. Richard, G. B. Rieker, C. Röske, S. W. Sharpe, E. Starikova, N. Stolarczyk, A. V. Stolyarov, K. Sung, F. Tamassia, J. Terragni, V. G. Ushakov, S. Vasilchenko, B. Vispoel, K. L. Vodopyanov, G. Wagner, S. Wójtewicz, S. N. Yurchenko, and N. F. Zobov, “The HITRAN2024 molecular spectroscopic database,” *J. Quant. Spectrosc. Radiat. Transfer* **353**, 109807 (2026).
- [45] T. Furtenbacher, R. Tóbiás, J. Tennyson, O. L. Polyansky, and A. G. Császár, “W2020: A database of validated rovibrational experimental transitions and empirical energy levels of H<sub>2</sub><sup>16</sup>O,” *J. Phys. Chem. Ref. Data* **49**, 033101 (2020).
- [46] T. Furtenbacher, R. Tóbiás, J. Tennyson, O. L. Polyansky, A. A. Kyuberis, R. I. Ovsyannikov, N. F. Zobov, and A. G. Császár, “The W2020 database of validated rovibrational experimental transitions and empirical energy levels of water isotopologues. II. H<sub>2</sub><sup>17</sup>O and H<sub>2</sub><sup>18</sup>O with an update to H<sub>2</sub><sup>16</sup>O,” *J. Phys. Chem. Ref. Data* **49**, 043103 (2020).

- [47] T. Furtenbacher, P. A. Coles, J. Tennyson, S. N. Yurchenko, S. Yu, B. Drouin, R. Tóbiás, and A. G. Császár, “Empirical rovibrational energy levels of ammonia up to  $7500\text{ cm}^{-1}$ ,” *J. Quant. Spectrosc. Radiat. Transf.* **251**, 107027 (2020).
- [48] M. Szczepanik, Á. Nagy, and E. Žak, “Simulating high-accuracy nuclear motion Hamiltonians in discrete variable representation using Walsh-Hadamard QROM with fault-tolerant quantum computers,” (2025), arXiv:2510.19062 [quant-ph].
- [49] K. Kanno, M. Kohda, R. Imai, S. Koh, K. Mitarai, W. Mizukami, and Y. O. Nakagawa, “Quantum-selected configuration interaction: classical diagonalization of Hamiltonians in subspaces selected by quantum computers,” (2023), arXiv:2302.11320 [quant-ph].
- [50] Y. O. Nakagawa, M. Kamoshita, W. Mizukami, S. Sudo, and Y.-y. Ohnishi, “ADAPT-QSCI: Adaptive construction of an input state for quantum-selected configuration interaction,” *J. Chem. Theory Comput.* **20**, 10817 (2024).
- [51] Quantinuum Reimei, <https://docs.quantinuum.com/systems/serenity/hardware/user-guide/performance-validation> (2024).
- [52] A. Bauder, “Fundamentals of rotational spectroscopy,” in *Handbook of High-resolution Spectroscopy*, edited by M. Quack and F. Merkt (Wiley, Hoboken, NJ, USA, 2011) pp. 57–116.
- [53] B. T. Darling and D. M. Dennison, “The water vapor molecule,” *Phys. Rev.* **57**, 128 (1940).
- [54] J. K. Watson, “Simplification of the molecular vibration-rotation hamiltonian,” *Mol. Phys.* **15**, 479 (1968).
- [55] C. Hampel, K. A. Peterson, and H.-J. Werner, “A comparison of the efficiency and accuracy of the quadratic configuration interaction (QCISD), coupled cluster (CCSD), and brueckner coupled cluster (BCCD) methods,” *Chem. Phys. Lett.* **190**, 1 (1992).
- [56] M. J. Deegan and P. J. Knowles, “Perturbative corrections to account for triple excitations in closed and open shell coupled cluster theories,” *Chem. Phys. Lett.* **227**, 321 (1994).
- [57] T. H. Dunning, Jr., “Gaussian basis sets for use in correlated molecular calculations. I. The atoms boron through neon and hydrogen,” *J. Chem. Phys.* **90**, 1007 (1989).
- [58] R. A. Kendall, T. H. Dunning, Jr., and R. J. Harrison, “Electron affinities of the first-row atoms revisited. Systematic basis sets and wave functions,” *J. Chem. Phys.* **96**, 6796 (1992).
- [59] H.-J. Werner, P. J. Knowles, P. Celani, W. Györffy, A. Hesselmann, D. Kats, G. Knizia, A. Köhn, T. Korona, D. Kreplin, R. Lindh, Q. Ma, F. R. Manby, A. Mitrushenkov, G. Rauhut, M. Schütz, K. R. Shamasundar, T. B. Adler, R. D. Amos, S. J. Bennie, A. Bernhardsson, A. Berning, J. A. Black, P. J. Bygrave, R. Cimiraglia, D. L. Cooper, D. Coughtrie, M. J. O. Deegan, A. J. Dobbyn, K. Doll, M. Dornbach, F. Eckert, S. Erfort, E. Goll, C. Hampel, G. Hetzer, J. G. Hill, M. Hodges, T. Hrenar, G. Jansen, C. Köppl, C. Kollmar, S. J. R. Lee, Y. Liu, A. W. Lloyd, R. A. Mata, A. J. May, B. Mussard, S. J. McNicholas, W. Meyer, T. F. Miller III, M. E. Mura, A. Nicklass, D. P. O’Neill, P. Palmieri, D. Peng, K. A. Peterson, K. Pflüger, R. Pitzer, I. Polyak, M. Reiher, J. O. Richardson, J. B. Robinson, B. Schröder, M. Schwilk, T. Shiozaki, M. Sibaev, H. Stoll, A. J. Stone, R. Tarroni, T. Thorsteinsson, J. Toulouse, M. Wang, M. Welborn, and B. Ziegler, “MOLPRO, version 2025.1, a package of ab initio programs,” [www.molpro.net](http://www.molpro.net).
- [60] H.-J. Werner, P. J. Knowles, G. Knizia, F. R. Manby, and M. Schütz, “Molpro: a general-purpose quantum chemistry program package,” *WIREs Comput. Mol. Sci.* **2**, 242 (2011).
- [61] H.-J. Werner, P. J. Knowles, F. R. Manby, J. A. Black, K. Doll, A. Hesselmann, D. Kats, A. Köhn, T. Korona, D. A. Kreplin, Q. Ma, T. F. Miller, A. Mitrushchenkov, K. A. Peterson, I. Polyak, G. Rauhut, and M. Sibaev, “The Molpro quantum chemistry package,” *J. Chem. Phys.* **152**, 144107 (2020).
- [62] R. Ramakrishnan and G. Rauhut, “Semi-quartic force fields retrieved from multi-mode expansions: Accuracy, scaling behavior, and approximations,” *J. Chem. Phys.* **142**, 154118 (2015).
- [63] N. P. D. Sawaya, T. Menke, T. H. Kyaw, S. Johri, A. Aspuru-Guzik, and G. G. Guerreschi, “Resource-efficient digital quantum simulation of  $d$ -level systems using qubit hardware,” *Quantum Inf. Process.* **19**, 1 (2020).
- [64] M. Hanada, S. Matsuura, E. Mendicelli, and E. Rinaldi, “Exponential improvement in quantum simulations of bosons,” (2025), arXiv:2505.02553 [quant-ph].
- [65] M. Mikkelsen and H. O. Valencia, “First and second quantized digital quantum simulations of bosonic systems,” (2025), arXiv:2511.10124 [quant-ph].
- [66] L. Hantzko, L. Binkowski, and S. Gupta, “Tensorized Pauli decomposition algorithm,” *Phys. Scr.* **99**, 085128 (2024).
- [67] E. Lötstedt and K. Yamanouchi, “Comparison of encoding schemes for quantum computing of  $S > 1/2$  spin chains,” *Phys. Rev. A* **111**, 062416 (2025).
- [68] A. Peruzzo, J. McClean, P. Shadbolt, M.-H. Yung, X.-Q. Zhou, P. J. Love, A. Aspuru-Guzik, and J. L. O’Brien, “A variational eigenvalue solver on a photonic quantum processor,” *Nat. Commun.* **5**, 4213 (2014).
- [69] X. Yuan, S. Endo, Q. Zhao, Y. Li, and S. C. Benjamin, “Theory of variational quantum simulation,” *Quantum* **3**, 191 (2019).
- [70] Y. Li, J. Hu, X.-M. Zhang, Z. Song, and M.-H. Yung, “Variational quantum simulation for quantum chemistry,” *Adv. Theory Simul.* **2**, 1800182 (2019).
- [71] M. Cerezo, A. Arrasmith, R. Babbush, S. C. Benjamin, S. Endo, K. Fujii, J. R. McClean, K. Mitarai, X. Yuan, L. Cincio, and P. J. Coles, “Variational quantum algorithms,” *Nat. Rev. Phys.* **3**, 625 (2021).
- [72] B. Reggio, N. Butt, A. Lytle, and P. Draper, “Fast partitioning of Pauli strings into commuting families for optimal expectation value measurements of dense operators,” *Phys. Rev. A* **110**, 022606 (2024).
- [73] Q.-S. Li, H.-Y. Liu, Q. Wang, Y.-C. Wu, and G.-P. Guo, “A unified framework of transformations based on the Jordan-Wigner transformation,” *J. Chem. Phys.* **157**, 134104 (2022).
- [74] E. R. Davidson, “The iterative calculation of a few of the lowest eigenvalues and corresponding eigenvectors of large real-symmetric matrices,” *J. Comput. Phys.* **17**, 87 (1975).
- [75] C. Lanczos, “An iteration method for the solution of the eigenvalue problem of linear differential and integral operators,” *J. Res. Natl. Bur. Stand.* **45**, 255 (1950).

- [76] E. Xu, W. Dawson, H. Pathak, and T. Nakajima, “Tensor-product bitstring selected configuration interaction,” (2025), arXiv:2503.10335 [physics.chem-ph].
- [77] M. Mikkelsen and Y. O. Nakagawa, “Quantum-selected configuration interaction with time-evolved state,” *Phys. Rev. Res.* **7**, 043043 (2025).
- [78] K. Sugisaki, S. Kanno, T. Itoko, R. Sakuma, and N. Yamamoto, “Hamiltonian simulation-based quantum-selected configuration interaction for large-scale electronic structure calculations with a quantum computer,” *Phys. Chem. Chem. Phys.* **27**, 20869 (2025).
- [79] J. Yu, J. R. Moreno, J. T. Iosue, L. Bertels, D. Claudino, B. Fuller, P. Groszkowski, T. S. Humble, P. Jurcevic, W. Kirby, T. A. Maier, M. Motta, B. Pokharel, A. Seif, A. Shehata, K. J. Sung, M. C. Tran, V. Tripathi, A. Mezzacapo, and K. Sharma, “Quantum-centric algorithm for sample-based Krylov diagonalization,” (2025), arXiv:2501.09702 [quant-ph].
- [80] K. Yamamoto, R. Masui, T. Nakajima, M. Tsuji, M. Sato, P. Schow, L. Heidemann, M. Burke, P. Seitz, O. J. Backhouse, J. W. Pedersen, J. Children, C. Holliman, N. Lysne, D. Okuno, S. Sivarajah, D. Muñoz Ramo, A. Chernoguzov, and R. Duncan, “Quantum-HPC hybrid computation of biomolecular excited-state energies,” arXiv:2601.15677 [quant-ph] (2026).
- [81] H. F. Trotter, “On the product of semi-groups of operators,” *Proc. Amer. Math. Soc.* **10**, 545 (1959).
- [82] M. Suzuki, “Generalized Trotter’s formula and systematic approximants of exponential operators and inner derivations with applications to many-body problems,” *Commun. Math. Phys.* **51**, 183 (1976).
- [83] J. Ostmeyer, “Optimised Trotter decompositions for classical and quantum computing,” *J. Phys. A: Math. Theor.* **56**, 285303 (2023).
- [84] E. Mátyus, C. Fábri, T. Szidarovszky, G. Czakó, W. D. Allen, and A. G. Császár, “Assigning quantum labels to variationally computed rotational-vibrational eigenstates of polyatomic molecules,” *J. Chem. Phys.* **133**, 034113 (2010).
- [85] R. D. Amos, N. C. Handy, W. H. Green, D. Jayatilaka, A. Willetts, and P. Palmieri, “Anharmonic vibrational properties of CH<sub>2</sub>F<sub>2</sub>: A comparison of theory and experiment,” *J. Chem. Phys.* **95**, 8323–8336 (1991).
- [86] A. L. L. East, W. D. Allen, and S. J. Klippenstein, “The anharmonic force field and equilibrium molecular structure of ketene,” *J. Chem. Phys.* **102**, 8506–8532 (1995).
- [87] A. G. Császár and I. M. Mills, “Vibrational energy levels of water,” *Spectrochim. Acta. A* **53**, 1101 (1997).
- [88] G. Czakó, T. Furtenbacher, A. G. Császár, and V. Szalay, “Variational vibrational calculations using high-order anharmonic force fields,” *Mol. Phys.* **102**, 2411 (2004).
- [89] E. Mátyus, G. Czakó, B. T. Sutcliffe, and A. G. Császár, “Vibrational energy levels with arbitrary potentials using the Eckart-Watson Hamiltonians and the discrete variable representation,” *J. Chem. Phys.* **127**, 084102 (2007).
- [90] J. M. Pino, J. M. Dreiling, C. Figgatt, J. P. Gaebler, S. A. Moses, M. S. Allman, C. H. Baldwin, M. Foss-Feig, D. Hayes, K. Mayer, C. Ryan-Anderson, and B. Neyenhuis, “Demonstration of the trapped-ion quantum CCD computer architecture,” *Nature* **592**, 209 (2021).
- [91] “Quantinuum Nexus,” (2024), <https://nexus.quantinuum.com/>.
- [92] S. Sivarajah, S. Dilkes, A. Cowtan, W. Simmons, A. Edgington, and R. Duncan, “t|ket>: a retargetable compiler for NISQ devices,” *Quantum Sci. Technol.* **6**, 014003 (2020).
- [93] R. Yoshida, E. Lötstedt, and K. Yamanouchi, “Quantum computing of Hückel molecular orbitals of  $\pi$ -electron systems,” *J. Chem. Phys.* **156**, 184117 (2022).
- [94] Z. Cai, R. Babbush, S. C. Benjamin, S. Endo, W. J. Huggins, Y. Li, J. R. McClean, and T. E. O’Brien, “Quantum error mitigation,” *Rev. Mod. Phys.* **95**, 045005 (2023).
- [95] Y. Ato, Y. Tachikawa, R. Yoshida, E. Lötstedt, and K. Yamanouchi, “Quantum computing of Hückel molecular orbitals of linear polyenes,” *Chem. Phys. Lett.* **877**, 142276 (2025).
- [96] P.-O. Löwdin, “On the nonorthogonality problem,” *Adv. Quantum Chem.* **5**, 185 (1970).
- [97] B. Huron, J. P. Malrieu, and P. Rancurel, “Iterative perturbation calculations of ground and excited state energies from multiconfigurational zeroth-order wavefunctions,” *J. Chem. Phys.* **58**, 5745 (1973).
- [98] A. A. Holmes, N. M. Tubman, and C. J. Umrigar, “Heat-bath configuration interaction: An efficient selected configuration interaction algorithm inspired by heat-bath sampling,” *J. Chem. Theory Comput.* **12**, 3674 (2016).
- [99] C. Ryan-Anderson, J. G. Bohnet, K. Lee, D. Gresh, A. Hankin, J. P. Gaebler, D. Francois, A. Chernoguzov, D. Lucchetti, N. C. Brown, T. M. Gatterman, S. K. Halit, K. Gilmore, J. A. Gerber, B. Neyenhuis, D. Hayes, and R. P. Stutz, “Realization of real-time fault-tolerant quantum error correction,” *Phys. Rev. X* **11**, 041058 (2021).
- [100] Quantinuum emulators: noise model, [https://docs.quantinuum.com/systems/user\\_guide/emulators/](https://docs.quantinuum.com/systems/user_guide/emulators/) (2025).
- [101] T. Halverson and B. Poirier, “One million quantum states of benzene,” *J. Phys. Chem. A* **119**, 12417 (2015).
- [102] S. Wang, “Intrinsic molecular vibration and rigorous vibrational assignment of benzene by first-principles molecular dynamics,” *Sci. Rep.* **10**, 17875 (2020).
- [103] K. Yagi and B. Thomsen, “Infrared spectra of protonated water clusters, H<sup>+</sup>(H<sub>2</sub>O)<sub>4</sub>, in Eigen and Zundel forms studied by vibrational quasi-degenerate perturbation theory,” *J. Phys. Chem. A* **121**, 2386 (2017).
- [104] Y. Zhang, Y. Wang, X. Xu, Z. Chen, and Y. Yang, “Vibrational spectra of highly anharmonic water clusters: Molecular dynamics and harmonic analysis revisited with constrained nuclear-electronic orbital methods,” *J. Chem. Theory Comput.* **19**, 9358 (2023).
- [105] I. Simkó, P. M. Felker, and Z. Bačić, “H<sub>2</sub>O trimer: Rigorous 12d quantum calculations of intermolecular vibrational states, tunneling splittings, and low-frequency spectrum,” *J. Chem. Phys.* **162**, 034301 (2025).
- [106] E. Lötstedt and T. Szidarovszky, “Rovibrational energy levels of H<sub>2</sub>O by quantum computing,” Zenodo dataset (2026), doi:10.5281/zenodo.18754103.
- [107] C. Eckart, “Some studies concerning rotating axes and polyatomic molecules,” *Phys. Rev.* **47**, 552 (1935).
- [108] S. A. Moses, C. H. Baldwin, M. S. Allman, R. Ancona, L. Ascarrunz, C. Barnes, J. Bartolotta, B. Bjork, P. Blanchard, M. Bohn, J. G. Bohnet, N. C. Brown,

N. Q. Burdick, W. C. Burton, S. L. Campbell, J. P. Campora, C. Carron, J. Chambers, J. W. Chan, Y. H. Chen, A. Chernoguzov, E. Chertkov, J. Colina, J. P. Curtis, R. Daniel, M. DeCross, D. Deen, C. Delaney, J. M. Dreiling, C. T. Ertsgaard, J. Esposito, B. Estey, M. Fabrikant, C. Figgatt, C. Foltz, M. Foss-Feig, D. Francois, J. P. Gaebler, T. M. Gatterman, C. N. Gilbreth, J. Giles, E. Glynn, A. Hall, A. M. Hankin, A. Hansen, D. Hayes, B. Higashi, I. M. Hoffman, B. Horning, J. J. Hout, R. Jacobs, J. Johansen, L. Jones, J. Karcz, T. Klein, P. Lauria, P. Lee, D. Liefer, S. T. Lu,

D. Lucchetti, C. Lytle, A. Malm, M. Matheny, B. Mathewson, K. Mayer, D. B. Miller, M. Mills, B. Neyenhuis, L. Nugent, S. Olson, J. Parks, G. N. Price, Z. Price, M. Pugh, A. Ransford, A. P. Reed, C. Roman, M. Rowe, C. Ryan-Anderson, S. Sanders, J. Sedlacek, P. Shevchuk, P. Siegfried, T. Skripka, B. Spaun, R. T. Sprenkle, R. P. Stutz, M. Swallows, R. I. Tobey, A. Tran, T. Tran, E. Vogt, C. Volin, J. Walker, A. M. Zolot, and J. M. Pino, "A race-track trapped-ion quantum processor," *Phys. Rev. X* **13**, 041052 (2023).